J. Fluid Mech. (2014), *vol.* 738, *pp.* 184–221. © Cambridge University Press 2013
doi:10.1017/jfm.2013.545

Flow instabilities in the wide-gap spherical Couette system

Johannes Wicht†

Max-Planck-Institut für Sonnensystemforschung, Katlenburg-Lindau, Germany

(Received 5 March 2013; revised 13 August 2013; accepted 11 October 2013;
first published online 5 December 2013)

The spherical Couette system is a spherical shell filled with a viscous fluid. Flows are driven by the differential rotation between the inner and the outer boundary that rotate with Ω and $\Omega + \Delta\Omega$ about a common axis. This setup has been proposed for second-generation dynamo experiments. We numerically explore the different instabilities emerging for rotation rates up to $\Omega = (1/3) \times 10^7$, venturing also into the nonlinear regime where oscillatory and chaotic solutions are found. The results provide a comprehensive overview of the possible flow regimes. For low values of Ω viscosity dominates and an equatorial jet in meridional circulation and zonal flow develops that becomes unstable as the differential rotation is increased beyond a critical value. For intermediate Ω and an inner boundary rotating slower than the outer one, new double-roll and helical instabilities are found. For large Ω values Coriolis effects enforce a nearly two-dimensional fundamental flow where a Stewartson shear layer develops at the tangent cylinder. This shear layer is the source of nearly geostrophic non-axisymmetric instabilities that resemble columnar Rossby modes. At first, the instabilities differ significantly depending on whether the inner boundary rotates faster ($\Delta\Omega > 0$) or slower ($\Delta\Omega < 0$) than the outer one. For very large outer boundary rotation rates, however, both instabilities once more become comparable. Fast inertial waves similar to those observed in recent spherical Couette experiments prevail for larger Ω values and $\Delta\Omega < 0$ in when $\Delta\Omega$ and Ω are of comparable magnitude. For larger differential rotations $\Delta\Omega \gg \Omega$, however, the equatorial jet instability always takes over.

Key words: free shear layers, instability, rotating flows

1. Introduction

The spherical Couette system is a spherical shell filled with a viscous fluid where flows are driven by the differential rotation $\Delta\Omega$ between the two boundaries about the common z-axis. The setup is in principle similar to the more widely explored cylindrical Couette–Taylor system (see Tagg 1994 for a review) and the instabilities are indeed comparable provided the aspect ratio is large so that the boundary curvature plays a less significant role (Egbers & Rath 1995). For smaller to intermediate aspect ratios, however, the first instabilities are already drastically different and the classical axisymmetric Taylor rolls give way to more complex non-axisymmetric modes (Buehler 1990; Egbers & Rath 1995) which are the topic of this paper.

† Email address for correspondence: wicht@mps.mpg.de

https://doi.org/10.1017/jfm.2013.545 Published online by Cambridge University Press

The spherical Couette setup has been proposed for second-generation dynamo experiments. Its geometry resembles planetary dynamo regions and some of the flow instabilities are reminiscent of convective columns. Two realizations are currently being explored: a large system with a diameter of 3 m (Zimmerman, Triana & Lathrop 2011) and a smaller system with 42 cm diameter (Brito *et al.* 2011). When filled with liquid sodium the larger experiment may actually operate as a dynamo. In the smaller experiment the inner core is a permanent magnet which at least allows the study of the effect of Lorentz forces. Several numerical studies explore the dynamics and dynamo action in these magnetic spherical Couette systems (Dormy, Cardin & Jault 1998; Schaeffer & Cardin 2006; Hollerbach 2009; Guervilly & Cardin 2010; Cao *et al.* 2012; Wei, Jackson & Hollerbach 2012; Figueroa *et al.* 2013).

This study concentrates on non-magnetic instabilities in a wide-gap container with an intermediate aspect ratio where boundary curvature effects become important. Previous numerical and experimental studies show that the outer boundary rotation rate Ω has a decisive influence on the flow instabilities (Egbers & Rath 1995; Hollerbach 2003; Hollerbach *et al.* 2004; Hollerbach, Junk & Egbers 2006). When the outer boundary is at rest, an outward directed radial jet develops in the equatorial plane and eventually becomes unstable to a non-axisymmetric instability (Hollerbach *et al.* 2006). Guervilly & Cardin (2010) demonstrate that this behaviour is still viable for moderate Ω values. When Ω is large, the basic flow is determined by Coriolis forces and approaches a quasi-two-dimensional geostrophic solution where variations along the rotation axis are minimized. The Stewartson shear layer that develops at the tangent cylinder that touches the inner core equator (Stewartson 1966) now becomes the source for the first non-axisymmetric instabilities. Hollerbach (2003) and Schaeffer & Cardin (2005) show that these instabilities differ for super- and sub-rotation, i.e. for cases where the inner boundary rotates faster or slower than the outer boundary, respectively.

Experiments and numerical simulations at more supercritical parameters suggest that inertial modes can also play an important role in the spherical Couette system (Kelley *et al.* 2007; Matsui *et al.* 2011; Rieutord *et al.* 2012). They form a class of natural solutions in fast rotating spheres and can thus be expected for larger Ω values (Greenspan 1968; Rieutord & Valdettaro 1997). The role of inertial modes in the spherical Couette system is further explored here.

The goal of this paper is to vary the inner and outer boundary rotation rates as much as the numerical power permits in order to provide a comprehensive regime overview. Varying the outer boundary rotation from zero to values beyond those reached by previous publications allows an outline of the regimes of equatorial jet and Stewartson layer instabilities and an exploration of what lies in between. The differential rotation is significantly increased beyond the onset of the first instability to study the nonlinear regime with its more complex spatial structures and time dependence. Section 2 introduces the numerical model, § 3 presents the numerical results and § 4 offers some concluding remarks. The Appendix is devoted to an analytical solution used to test the code.

2. Model formulation

We explore the flow in the spherical Couette system by numerically solving the Navier–Stokes equation in a frame of reference corotating with the outer boundary. When using the distance between the outer boundary of radius r_o and the inner boundary of radius r_i as a length scale $L = r_o - r_i$ and the viscous diffusion time L^2/ν

https://doi.org/10.1017/jfm.2013.545 Published online by Cambridge University Press

as a time scale the dimensionless Navier–Stokes equation reads

$$\frac{\partial \boldsymbol{U}}{\partial t} = -\boldsymbol{U}\cdot\boldsymbol{\nabla}\boldsymbol{U} - \boldsymbol{\nabla} p - 2\Omega\hat{\boldsymbol{z}}\times\boldsymbol{U} + \nabla^2\boldsymbol{U}. \tag{2.1}$$

Here, ν is the kinematic viscosity, $\boldsymbol{U}$ the dimensionless velocity, p a modified dimensionless pressure also containing centrifugal forces due to rotation Ω, and $\hat{\boldsymbol{z}}$ the unit vector in the direction of the rotation axis. For the incompressible flow assumed here, $\boldsymbol{U}$ obeys the simplified continuity equation

$$\boldsymbol{\nabla}\cdot\boldsymbol{U} = 0, \tag{2.2}$$

which is automatically fulfilled by using the poloidal/toroidal decomposition

$$\boldsymbol{U} = \boldsymbol{\nabla}\times\boldsymbol{\nabla}\times\hat{\boldsymbol{r}}U_P + \boldsymbol{\nabla}\times\hat{\boldsymbol{r}}U_T \tag{2.3}$$

with poloidal potential U_P and toroidal potential U_T. Here $\hat{r}$ is the radial unit vector.

The system is governed by three non-dimensional numbers: the outer boundary rotation rate

$$\Omega = \frac{\Omega_o L^2}{\nu}, \tag{2.4}$$

the differential rotation

$$\Delta\Omega = \frac{(\Omega_i - \Omega_o)L^2}{\nu}, \tag{2.5}$$

and the aspect ratio $a = r_i/r_o$. Here, Ω_o and Ω_i are the dimensional rotation rates of inner and outer boundary, respectively. In the scaling chosen here, Ω is the inverse of the frequently used Ekman number E and provides a measure for the ratio of Coriolis to viscous forces. Flow amplitudes and rotation rates can be interpreted as Reynolds numbers.

Another dimensionless parameter that plays an important role in the dynamics of the spherical Couette system is the ratio of differential rotation to outer boundary rotation, typically referred to as the Rossby number in this context (Hollerbach 2003):

$$Ro = \Delta\Omega/\Omega. \tag{2.6}$$

In order to solve the above system numerically, the MHD code MagIC (Wicht 2002; Christensen & Wicht 2007) has been adapted by replacing buoyancy driving with imposed inner and outer boundary rotation rates. MagIC employs pseudo-spectral methods, using spherical harmonics for the lateral spectral representation and Chebychev polynomials in the radius (Glatzmaier 1984). Chebychev polynomials guarantee an increased resolution towards r_i and r_o where boundary layers need to be resolved. MagIC has been benchmarked for convection and dynamo action (Christensen *et al.* 2001), an analytical solution presented in § 3 and the Appendix serves to verify the viscous driving via the boundaries.

Keeping the aspect ratio a at 0.35, a value close to the Earth's core aspect ratio and to the two experiments mentioned in the introduction, we explore a wide range of Ω and $\Delta\Omega$ values. When increasing $\Delta\Omega$ or Ω both the length scales and the time scales decrease so that the numerical costs grow rapidly. The largest outer boundary rotation rate studied is $\Omega = (1/3)\times 10^7 (E = 3\times 10^{-7})$ which requires a resolution of $N_r = 161$ radial grid points and $N_\theta = 576$ colatitudinal grid points to guarantee that the kinetic energy is converged to within 1%, a precision generally found to be adequate.

https://doi.org/10.1017/jfm.2013.545 Published online by Cambridge University Press

At $N_\theta = 576$ the colatitude grid corresponds to a maximum spherical harmonic degree of $l = 384$ in the fully dealiased representation used here (Glatzmaier 1984).

The numerical strategy was the following: for a fixed outer boundary rotation rate Ω the differential rotation $\Delta\Omega$ is changed in small increments, spanning super-rotation cases with $\Delta\Omega > 0$ as well as sub-rotation cases with $\Delta\Omega < 0$. A non-axisymmetric solution with a full mode spectrum (spherical harmonic orders) serves as a starting point for gradually decreasing $\Delta\Omega$ to identify the most supercritical mode for the first non-axisymmetric and following instabilities. For $\Omega \leqslant 10^5$, the exploration of a larger range of differential rotation rates could be afforded, reaching well into the regime that shows chaotic time behaviour (see § 3). At more extreme Ω values, however, the numerical restriction allowed $\Delta\Omega$ to be increased only slightly beyond the onset of the first non-axisymmetric instability.

3. Results

Figure 1 provides an overview of the different regimes encountered during the parameter scan. For small values of $\Delta\Omega$ the flow is strictly axisymmetric but becomes unstable to a non-axisymmetric instability of wavenumber m_c once a critical value $\Delta\Omega_c$ is exceeded. This first instability simply drifts in azimuth with a fraction of $\Delta\Omega$, prograde for super-rotation $\Delta\Omega > 0$ and retrograde for sub-rotation $\Delta\Omega < 0$. A drifting solution obeys the simple azimuthal and time dependence $\exp(m\phi - \omega_d t)$ where ϕ is the azimuth and ω_d the drift rate. On further increasing $\Delta\Omega$ more wavenumbers set in, the spatial flow complexity increases and the solution becomes chaotic, mostly via a regime where mode interaction leads to oscillation in the r.m.s. flow amplitude. The values of m_c and $\Delta\Omega_c$ and also the type of instability depend on Ω. Both m_c and $\Delta\Omega_c$ are listed in table 1 along with a classification of the first non-axisymmetric instabilities.

For slow outer boundary rotation $\Omega \leqslant 1$ the first instability is the equatorial jet instability previously identified by Hollerbach (2003), Hollerbach *et al.* (2006) and Guervilly & Cardin (2010). For intermediate values $1 < \Omega < 10^3$, $\Delta\Omega > 0$ cases resemble moderately modified equatorial jet instabilities. For $\Delta\Omega < 0$, however, new double-roll and helical instabilities appear that have not been described before. Once Ω exceeds 10^3, Coriolis effects enforce a quasi-two-dimensional basic flow structure and the first instability is of the Stewartson type (Hollerbach 2003; Schaeffer & Cardin 2005) with an interesting difference between the sub-rotation and the super-rotation cases. This difference seems to vanish at least partly once Ω exceeds 3×10^5 which lies beyond the values previously explored by other authors. A mode cascade to smaller wavenumbers and the excitation of inertial modes are also typical for the large-Ω regime. The following sections describe the solution in the individual regimes including the basic axisymmetric flows and solutions in the nonlinear regime beyond $\Delta\Omega_c$. Section 3.4 is devoted to discussing the drift of the different instabilities and their relation to inertial modes.

3.1. *Slow outer boundary rotation:* $\Omega \leqslant 1$

For $\Omega < 1$ viscous effects play a more important role than the Coriolis force associated with the outer boundary rotation. The flow is therefore rather large scale, and shows no tendency to become z-independent. Figure 1 demonstrates that neither Ω nor the sign of $\Delta\Omega$ affect the onset of the first non-axisymmetric nor of any higher instabilities.

https://doi.org/10.1017/jfm.2013.545 Published online by Cambridge University Press

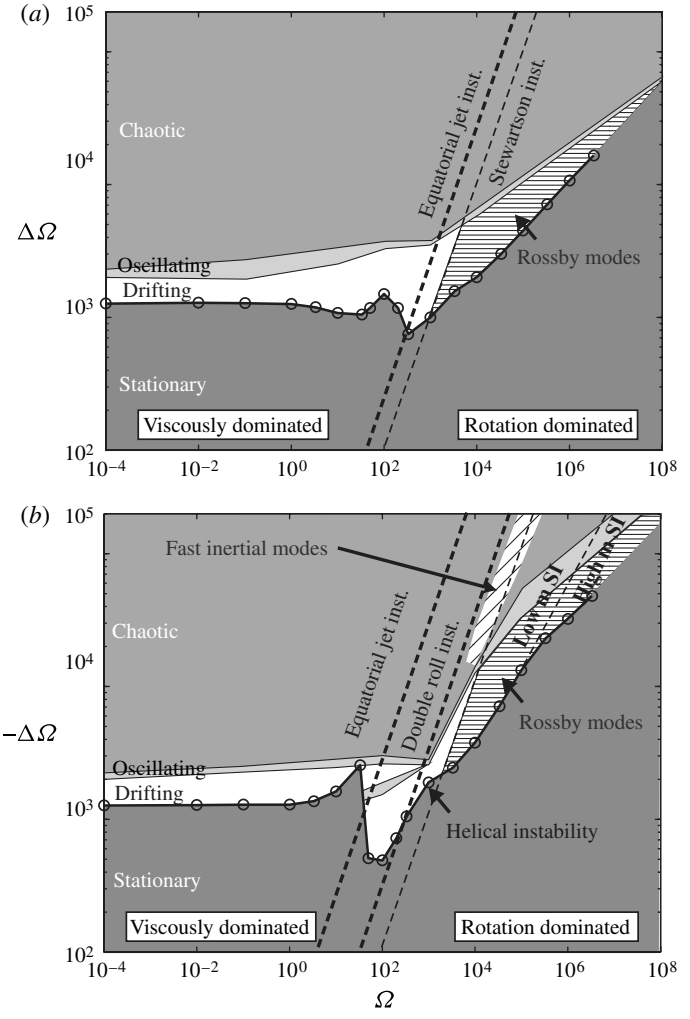


FIGURE 1. Regime diagrams for (*a*) super-rotation $\Delta\Omega > 0$ and (*b*) sub-rotation $\Delta\Omega < 0$ cases. Circles connected by thick lines show the critical differential rotation rates $\Delta\Omega_c$ for the onset of the first drifting non-axisymmetric instability. Below this line, only axisymmetric solutions exist. For small Ω, viscous forces dominate and the first instability is of the equatorial jet type. For large Ω, the flow becomes geostrophic and a Stewartson shear layer instability (SI) sets in first. The thin dashed lines mark $Ro = \Delta\Omega/\Omega = 1$. For large Ro values above the thick dashed lines, the equatorial jet instability becomes influential even at larger Ω. For $\Delta\Omega < 0$ distinct double-roll instabilities are found at intermediate Ω values between the two thick dashed lines. For large Ω and $Ro \approx 1$, equatorially antisymmetric inertial modes dominate the solution. For $\Omega > 10^5$ only the onset of the first non-axisymmetric instability has been determined and the other regime boundaries are educated guesses.

Figure 2 illustrates how the r.m.s. amplitudes of different flow contributions depend on $\Delta\Omega$. We have depicted the super-rotation case at $\Omega = 10^{-4}$ here, but equivalent diagrams for other small Ω values (including $\Omega = 0$) and also for the sub-rotation cases are practically identical. The total r.m.s. flow amplitude U, a Reynolds number in the scaling chosen here, grows nearly linearly with $\Delta\Omega$ over a wide range of

https://doi.org/10.1017/jfm.2013.545 Published online by Cambridge University Press

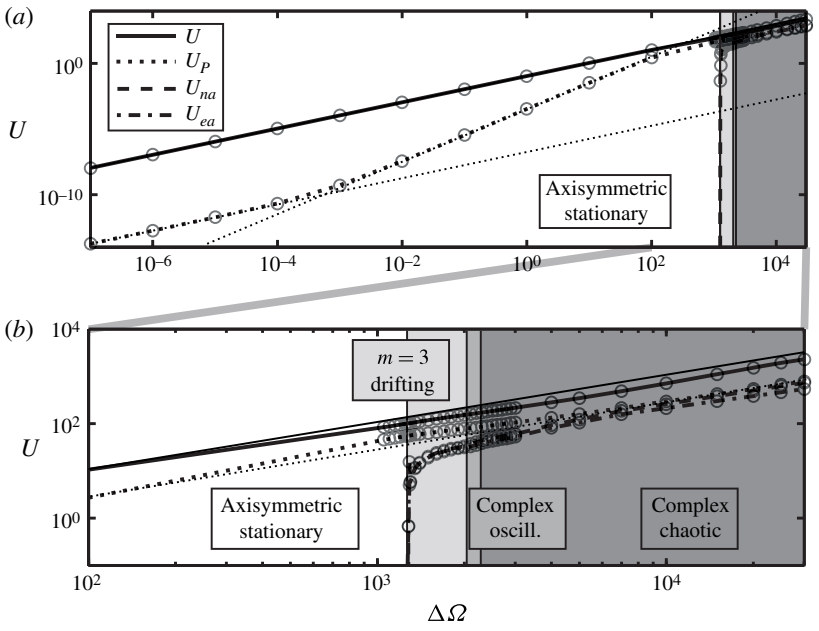


FIGURE 2. Dependence of different dimensionless flow amplitudes (Reynolds numbers) on the differential rotation rate $\Delta\Omega > 0$ at $\Omega = 10^{-4}$: (*b*) is a zoom of the larger-$\Delta\Omega$ end of (*a*). Thick solid lines show the total r.m.s. flow Reynolds number U which depends roughly linearly (indicated by the thin solid line) on $\Delta\Omega$. Thick dotted lines give the r.m.s. amplitude of the poloidal flow contribution U_P. As long as the flow remains axisymmetric this is identical to the amplitude of the meridional circulation. Thin dotted lines indicate a (theoretical) linear and quadratic dependence on $\Delta\Omega$. Thick dashed lines show the r.m.s. amplitude of the non-axisymmetric flow contribution U_{na} and thick dash-dotted lines provide the r.m.s. amplitude of the equatorially antisymmetric flow U_{ea}. The different regimes, including the time behaviour, are distinguished by different grey shades in the background. The azimuthal wavenumber (where relevant) and the time behaviour of each regime are indicated in the boxes. Complex refers to different incommensurable interacting wavenumbers. The diagram for $\Delta\Omega < 0$ is virtually identical except for a small region around $-\Delta\Omega = \Omega$ where the cancellation of the opposing Coriolis and advective driving leads to a small decrease in the poloidal flow amplitude (see text). Circles indicate the actual time-averaged values the lines are based on.

parameters. This can be expected for $Ro \ll 1$ as will be demonstrated below. The different regimes can more clearly be distinguished when analysing the r.m.s. poloidal flow amplitude U_P, the non-axisymmetric flow amplitude U_{na} or the equatorially antisymmetric contribution U_{ea}.

3.1.1. *Axisymmetric regime*

Three regimes can be distinguished even before the first non-axisymmetric instability sets in. Figure 2 shows that U_P first grows linearly with $\Delta\Omega$, then a quadratic regime with $U_P \sim \Delta\Omega^2$ is encountered and finally the growth rate approaches again a more linear behaviour. Figure 3 illustrates that the solutions in the first two regimes, represented by cases at $\Delta\Omega = 10^{-6}$ and $\Delta\Omega = 10$, are very similar and have a rather simple structure that can be assessed analytically, as will be shown in the following.

The differential rotation primarily drives axisymmetric zonal flows $\bar{U}_\phi$ via viscous friction. All other flow components rely on a conversion of this primary flow due to

https://doi.org/10.1017/jfm.2013.545 Published online by Cambridge University Press

https://doi.org/10.1017/jfm.2013.545 Published online by Cambridge University Press

Ω	$\Delta\Omega > 0$				$\Delta\Omega < 0$			
	$\Delta\Omega_c$	Ro_c	m_c	inst.	$\Delta\Omega_c$	Ro_c	m_c	inst.
0	1270 (1260)	∞	3	EJ, EA				
10^{-4}	1270 (1260)	1.27×10^{7}	3	EJ, EA	−1270 (−1260)	-1.26×10^{7}	3	EJ, EA
10^{-1}	1290 (1280)	1.29×10^{4}	3	EJ, EA	−1290 (−1280)	-1.29×10^{4}	3	EJ, EA
10^{0}	1260 (1250)	1.27×10^{3}	3	EJ, EA	−1290 (−1280)	-1.29×10^{3}	3	EJ, EA
10^{1}	1080 (1060)	1.08×10^{2}	2	EJ, EA	−1610 (−1600)	-1.16×10^{2}	3	EJ, EA
10^{2}	1500 (1450)	1.50×10^{1}	3	EJ, EA	−500 (−490)	−5.0	2	DR, EA
10^{3}	1010 (1000)	1.01	2	SL, geo.	−1900 (−1850)	−1.85	3	SL, hel.
10^{4}	2010 (2000)	2.01×10^{-1}	4	SL, geo.	−3790 (−3780)	-3.79×10^{-1}	1	SL, geo.
10^{5}	4500 (4400)	4.50×10^{-2}	8	SL, geo.	−13 300 (−13 100)	-1.33×10^{-1}	2	SL, geo.
$(1/3) \times 10^{6}$	7100 (7000)	2.37×10^{-2}	12	SL, geo.	−23 000 (−22 000)	-7.66×10^{-2}	12	SL, geo.
10^{6}	11 000 (10 750)	1.10×10^{-2}	17	SL, geo.	−34 000 (−33 000)	-3.40×10^{-2}	16	SL, geo.
$(1/3) \times 10^{7}$	16 600 (16 400)	5.33×10^{-3}	23	SL, geo.	−45 000 (−44 000)	-1.47×10^{-2}	24	SL, geo.

TABLE 1. Critical differential rotations rates $\Delta\Omega_c$ and azimuthal wavenumbers m_c for the onset of the first non-axisymmetric instability. The bracketed values are closest modelled differential rotation rates where the numerical simulations remained axisymmetric. Columns denoted inst. characterize the type of instability (EJ = equatorial jet, DR = double roll, SL = Stewartson layer) and its geometry (EA = equatorially antisymmetric, geo. = nearly geostrophic, hel. = helical). Drift rates for some of the instabilities are listed in table 2.

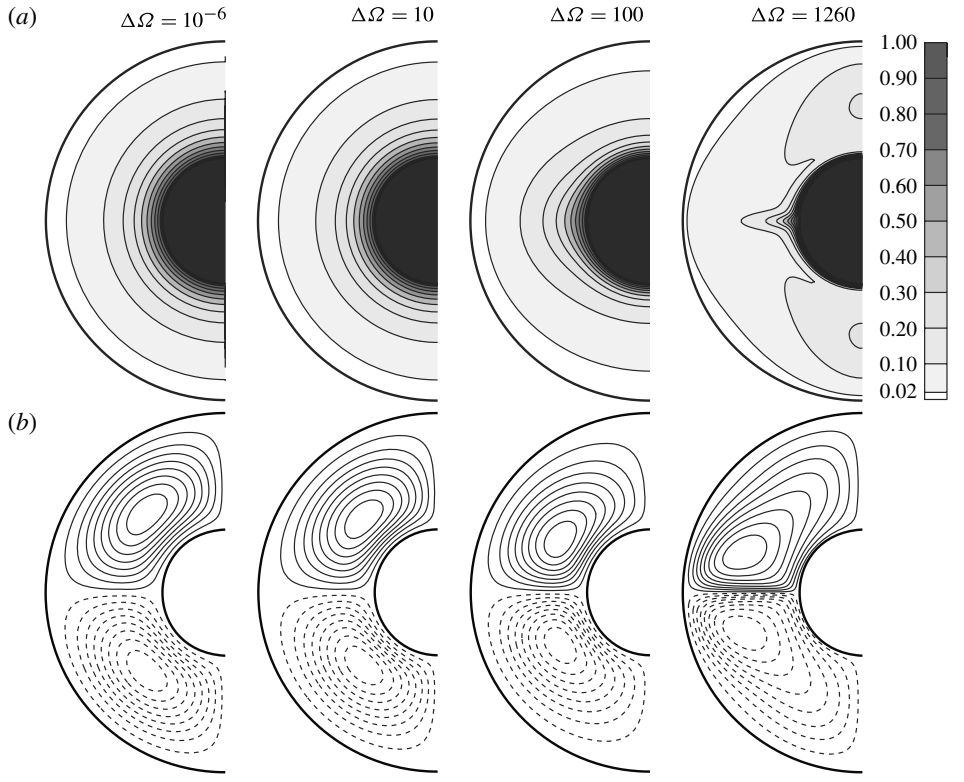


FIGURE 3. Axisymmetric flow at $\Omega = 10^{-4}$ for different values of differential rotation $\Delta\Omega$: (*a*) the normalized angular velocity $\bar{\omega}/\Delta\Omega$; (*b*) axisymmetric meridional streamlines, solid streamlines indicate clockwise flow and dashed anticlockwise. For $\Delta\Omega < 0$ the solution has the same structure but the direction of the angular velocity is reversed. The direction of the meridional circulation changes only when $\Delta\Omega < \Omega$ (see text).

the additional forces acting in the system. These components may thus be regarded as secondary, but can actually become comparable to the primary flow in amplitude for large values of $\Delta\Omega$. Below the critical differential rotation $\Delta\Omega_c$ the flow remains stationary and axisymmetric. The primary flow $\bar{U}_\phi$ is then the only toroidal flow component,

$$\boldsymbol{U}_T = \bar{U}_\phi \hat{\boldsymbol{\phi}}, \tag{3.1}$$

and the poloidal flow can be expressed via a stream function Ψ,

$$\boldsymbol{U}_P = \boldsymbol{\nabla} \times \hat{\boldsymbol{\phi}} \Psi, \tag{3.2}$$

describing the axisymmetric radial and latitudinal flow components $\bar{U}_r$ and $\bar{U}_\theta$.

The azimuthal component of the Navier–Stokes equation (2.1) provides an equation for $\bar{U}_\phi$:

$$\left(\frac{\bar{U}_r}{r} \frac{\partial}{\partial r} r + \frac{\bar{U}_\theta}{r \sin\theta} \frac{\partial}{\partial \theta} \sin\theta \right) \bar{U}_\phi = -2\Omega (\cos\theta \bar{U}_\theta + \sin\theta \bar{U}_r) + \hat{\boldsymbol{\phi}} \cdot \nabla^2 \bar{U}_\phi, \tag{3.3}$$

https://doi.org/10.1017/jfm.2013.545 Published online by Cambridge University Press

while the azimuthal component of the curl of the Navier–Stokes equation provides an equation for Ψ:

$$\left(\nabla^2 - \frac{1}{r^2\sin^2\theta}\right)^2 \Psi = \hat{\boldsymbol{\phi}} \cdot \nabla \times \left(\boldsymbol{U} \cdot \nabla \boldsymbol{U} + 2\Omega\hat{\boldsymbol{z}} \times \boldsymbol{U}\right). \tag{3.4}$$

Both equations formulate a balance between advection, Coriolis force and viscous diffusion.

For $\Omega \ll 1$ and a poloidal flow amplitude U_P that is significantly smaller than the toroidal flow amplitude U_T, i.e. $U_P/U_T \ll 1$, the leading order of (3.3) becomes linear and reduces to the purely viscous case:

$$\nabla^2 \bar{U}_\phi = 0. \tag{3.5}$$

This can be solved analytically subject to the boundary conditions imposed by the differential rotation and simply yields

$$\bar{U}_\phi = r\sin\theta\bar{\omega}, \tag{3.6}$$

with the flow angular velocity

$$\bar{\omega} = \frac{(r_i/r)^3 - a^3}{1 - a^3}\Delta\Omega. \tag{3.7}$$

As expected, the amplitude of the basic flow scales linearly with the differential rotation.

When using (3.7) the leading order of (3.4) reduces to

$$\left(\nabla^2 - \frac{1}{r^2\sin^2\theta}\right)^2 \Psi = 6\sin\theta\cos\theta\frac{(r_i/r)^3}{1 - a^3}\Delta\Omega\,(\Omega + \bar{\omega}). \tag{3.8}$$

This can also be solved analytically and the somewhat complex solution is given in the Appendix along with a demonstration of how the analytical flow has been used to verify the numerical code. Equation (3.8) shows that the meridional circulation is driven by centrifugal forces associated with the outer boundary rotation Ω or with the angular velocity ω induced by the imposed differential rotation $\Delta\Omega$. We refer to these two contributions as Coriolis and advective driving in the following.

For $|Ro| = |\Delta\Omega|/\Omega \ll 1$, Coriolis driving dominates and the poloidal flow amplitude U_P thus behaves like

$$U_P \sim \Delta\Omega\,\Omega. \tag{3.9}$$

Since then both the poloidal and the toroidal flow amplitudes increase linearly with $\Delta\Omega$ the condition $U_P/U_T \ll 1$ remains satisfied. The numerical results show that the ratio of these contribution is $U_P/U_T \approx 1.6 \times 10^{-2}\Omega$. Only the direction of the zonal and poloidal flow depends on the sign of $\Delta\Omega$ but not the structure. For $\Delta\Omega > 0$ the meridional circulation is outward in the equatorial plane and inward at high latitudes.

For $|Ro| \gg 1$, the advective driving dominates and the poloidal flow amplitude increases quadratically with $\Delta\Omega$,

$$U_P \sim \Delta\Omega^2. \tag{3.10}$$

The solution thus becomes independent of Ω. Since the poloidal flow amplitude now increases faster than the toroidal flow amplitude the condition $U_P/U_T \ll 1$ will be violated beyond some $\Delta\Omega$. Advection due to the poloidal flow then modifies the

https://doi.org/10.1017/jfm.2013.545 Published online by Cambridge University Press

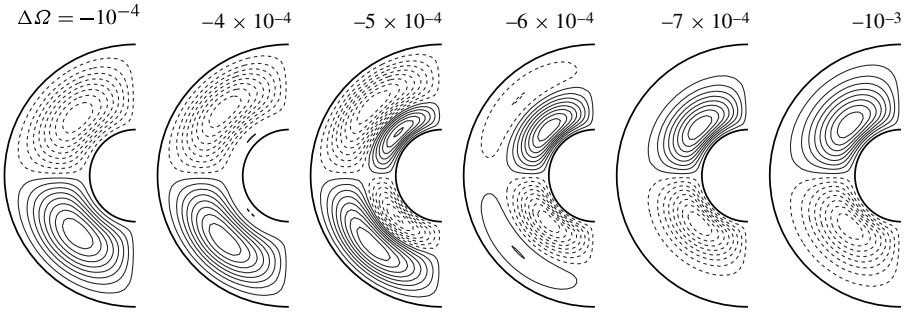


FIGURE 4. Development of the meridional circulation for $\Omega = 10^{-4}$ and $\Delta\Omega < 0$ as the absolute Rossby number $|Ro|$ increases beyond 1. $|Ro|$ values from left to right are 1, 4, 5, 6, 7 and 10.

solution and our analytical approach becomes invalid. The numerical results show that the ratio of the r.m.s. flow amplitudes scales like $U_P/U_T \approx 3 \times 10^{-3}\Delta\Omega$. A stronger influence of the poloidal flow is thus expected beyond $\Delta\Omega \approx 100$. Figure 2 demonstrates that this influence causes a decrease of the quadratic growth of U_P towards a more linear behaviour.

Figure 3 illustrates how the axisymmetric flow evolves on increasing $\Delta\Omega$ in the super-rotation case. A comparison of the panels for $\Delta\Omega = 10^{-6}$ and $\Delta\Omega = 10$ demonstrates that the centre of the meridional circulation cells moves slightly closer to the inner boundary as Ro is increased from $Ro = 10^{-2}$ to $Ro = 10^{5}$. The reason is that $\bar{\omega}$ and thus the advective driving that dominates in the latter case decrease with radius (see (3.7)). Around $\Delta\Omega \approx 100$ the advection along the inner boundary towards the equatorial plane and then outward starts to create a bulge in the angular velocity profile which develops into a progressively thinner equatorial jet. The form of the poloidal flow changes accordingly and develops a confined outward jet in the equatorial plane.

For $|Ro| \ll 1$ the flows in the super- and sub-rotation cases have the same structure but opposite directions but this changes around $|Ro| \approx 1$. The poloidal flow is driven due to Coriolis and advective effects and these operate in the same direction for $\Delta\Omega > 0$ but oppose each other for $\Delta\Omega < 0$. Figure 4 demonstrates that for $\Delta\Omega < 0$ the meridional circulation assumes a transitional double-roll structure with two counter-rotating cell pairs between $Ro = -1$ and $Ro = -10$. Since the efficiency of the advective driving decreases with radius the associated cells first appear near the inner boundary and gradually replace the cells due to Coriolis driving. Once the advective forcing clearly dominates for $|Ro| \geqslant 10$ super- and sub-rotation cases exhibit identical meridional circulation cells that rotate in the same direction since the advective forcing is quadratic in $\Delta\Omega$. As expected, the outer boundary rotation ceases to matter for $|Ro| \gg 1$ and the same non-axisymmetric instability sets in for both signs of $\Delta\Omega$ (see figure 1).

3.1.2. *Non-axisymmetric regime*

As $\Delta\Omega$ is increased the equatorial jet becomes thinner and thinner and ultimately becomes unstable at a critical value around $\Delta\Omega_c = 1270$ (see table 1). In the scaling chosen here, $\Delta\Omega_c$ has the form of a critical Reynolds number that should remain independent of Ω as long as the outer boundary rotation has no impact. The r.m.s. flow Reynolds number U is approximately 100 at onset, apparently large

https://doi.org/10.1017/jfm.2013.545 Published online by Cambridge University Press

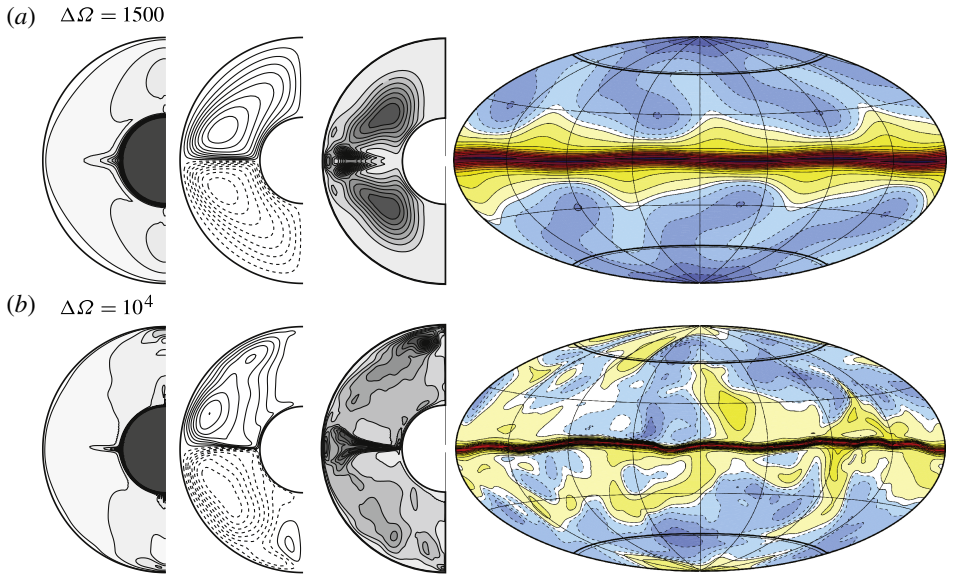


FIGURE 5. (Colour online) Visualization of the flows for $\Omega = 0$ representative of the slow-Ω regime. From left to right: normalized angular velocity, meridional circulation, azimuthally averaged non-axisymmetric kinetic energy and radial flow at mid depth $r_i + (r_o - r_i)/2$. The dashed contours (blue online) indicate radially inward directed flows and the solid contours (yellow to red online) radially outward directed flows. A white contour marks weak radial flow amplitudes within plus or minus 2 % of the absolute maximum.

enough for the instability to overcome viscosity. Figures 5 and 6 illustrate the somewhat more developed flow at $\Delta\Omega = 1500$. The instability has an azimuthal wavenumber $m = 3$ and is present throughout the shell. The radial equatorial jet assumes a wavy structure, undulating weakly around the equatorial plane. The non-axisymmetric instability is perfectly equatorially antisymmetric while the axisymmetric flow is equatorially symmetric. But when increasing $\Delta\Omega$ to more supercritical values, the non-axisymmetric flows also develop equatorially symmetric components (see figure 2). Poloidal and toroidal flow contributions have a comparable magnitude with $U_P/U_T \approx 0.5$ close to onset. Either the zonal jet or the outward directed jet in the meridional circulation may become unstable first. The whole solution drifts in the direction of inner sphere rotation but at a slower rate.

Around $\Delta\Omega = 2000$ an additional equatorial symmetric mode with wavenumber $m = 1$ sets in and drifts 20 % slower than the $m = 3$ mode. Nonlinear interactions excite all other wavenumbers and lead to a weak oscillation in the r.m.s. flow amplitude with a frequency of $\omega_f \approx 180$.

Oscillatory solutions generally occupy only a small fraction of the parameter space and are already superseded by chaotic solutions around $\Delta\Omega = 2400$. The chaotic time dependence is accompanied by a more complex spatial structure illustrated in figure 5 for $\Delta\Omega = 10^4$. Several different wavenumbers are excited and smaller-scale features emerge. The increased differential rotation promotes a yet thinner equatorial jet which becomes difficult to resolve numerically. While the drift remains the main time dependence, the relative contributions of the different wavenumbers also vary, leading to faster changes of particularly the smaller-scale features. The axisymmetric solution

https://doi.org/10.1017/jfm.2013.545 Published online by Cambridge University Press

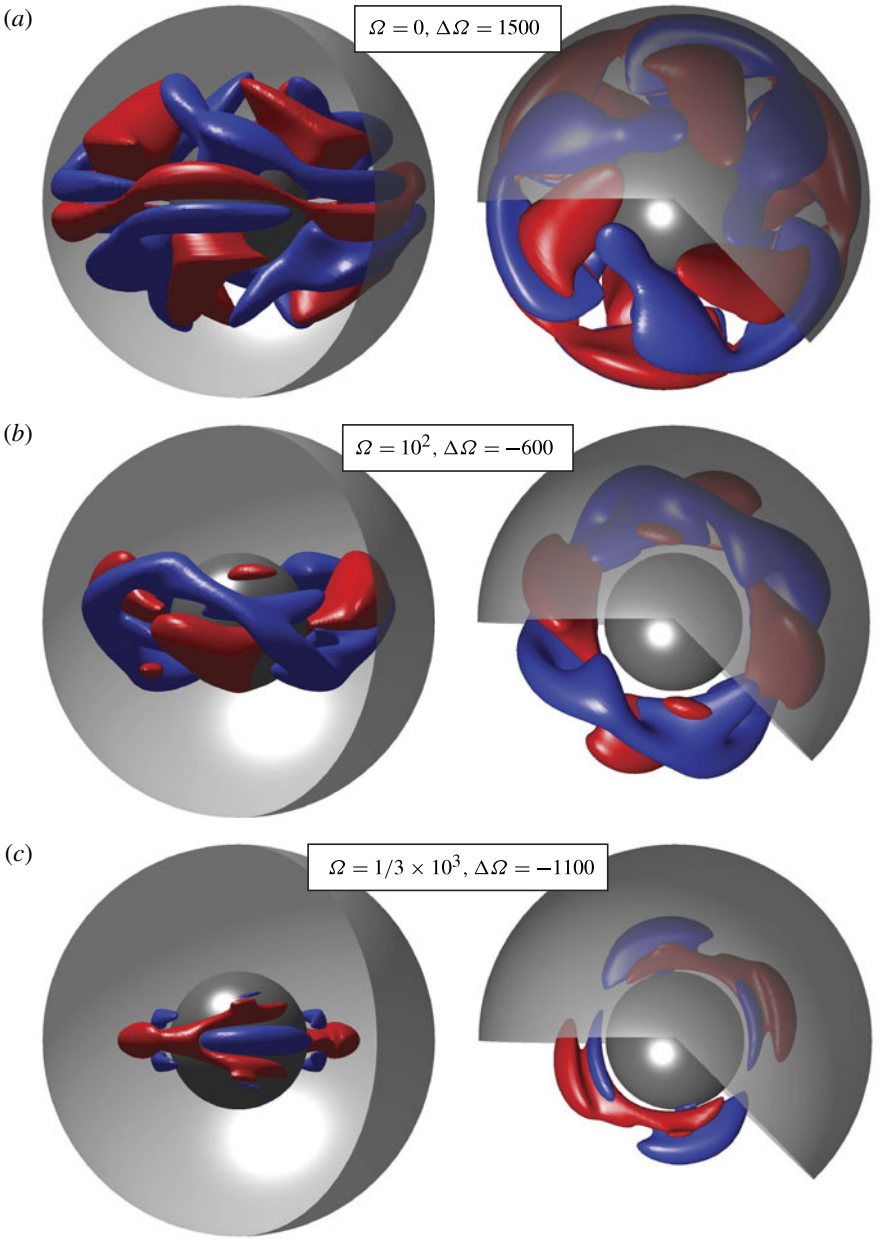


FIGURE 6. (Colour online) Isosurfaces of the non-axisymmetric outward (inward) radial flow in red online (blue online) for different parameter combinations: left panels show a view on the equator, and right panels a view on the north pole. This rendering further illustrates the solutions shown in figures 5 and 9.

keeps the basic structure shown in the snapshot in figure 5 but the relatively weak equatorially antisymmetric contributions change over time and are more variable inside than outside the tangent cylinder. The time-averaged solution is perfectly equatorially symmetric.

https://doi.org/10.1017/jfm.2013.545 Published online by Cambridge University Press

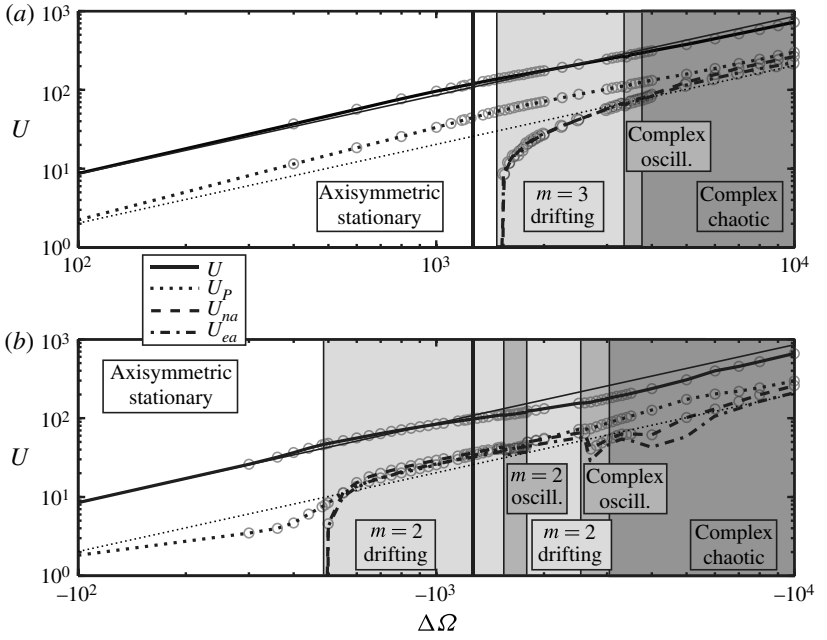


FIGURE 7. Dimensionless flow amplitudes (Reynolds numbers) for $\Omega = 10^2$ and (*a*) super-rotating or (*b*) sub-rotating inner boundary. Thick vertical lines mark the onset of the drifting non-axisymmetric instability for $\Omega \ll 1$. For more explanation see figure 2.

At $\Omega = 10^{-1}$ the solutions begin to differ slightly from those at smaller outer boundary rotation rates. The critical values for the onset of the instabilities are slightly shifted (see figure 1 and table 1) and the sign of $\Delta\Omega$ starts to matter. At $\Omega = 1$ the differences are somewhat larger but the general scenario described above still holds. This changes, however, when Ω is increased further.

3.2. *Intermediate outer boundary rotation:* $1 < \Omega < 10^3$

For super-rotation, the onset of the non-axisymmetric instability is first delayed as Ω increases, for example to $\Delta\Omega_c = 1500$ at $\Omega = 10^2$ (see figure 1 and table 1). However, the first non-axisymmetric as well as higher instabilities remain very similar to those found for slower outer boundary rotations. Figure 7 illustrates the regime diagram at $\Omega = 10^2$. At $\Omega = 2 \times 10^2$ the critical rotation rate starts to decrease and finally reaches the distinct fast outer boundary rotation branch described in § 3.3 at $\Omega = (1/3) \times 10^3$.

For sub-rotation, the critical value for the onset of the equatorial jet instability doubles to $\Delta\Omega_c = -2560$ when Ω is increased to $\Omega = (1/3) \times 10^2$ while the nature of the instability remains basically unchanged. At $\Omega = 10^2$, however, the presence of the double-roll background flow structure and related reversal of flow direction lead to a new instability. The double roll structure appears around $Ro = -1$ and thus for $\Delta\Omega \approx -100$ at $\Omega = 10^2$. This is close enough to the onset of the equatorial jet instability to become influential. Figure 8 illustrates that two effects modify the structure compared to the $\Omega = 10^{-4}$ cases shown in figure 4: the Coriolis force has started to impose a quasi-two-dimensional structure and the advective modification of zonal and meridional flow becomes important.

https://doi.org/10.1017/jfm.2013.545 Published online by Cambridge University Press

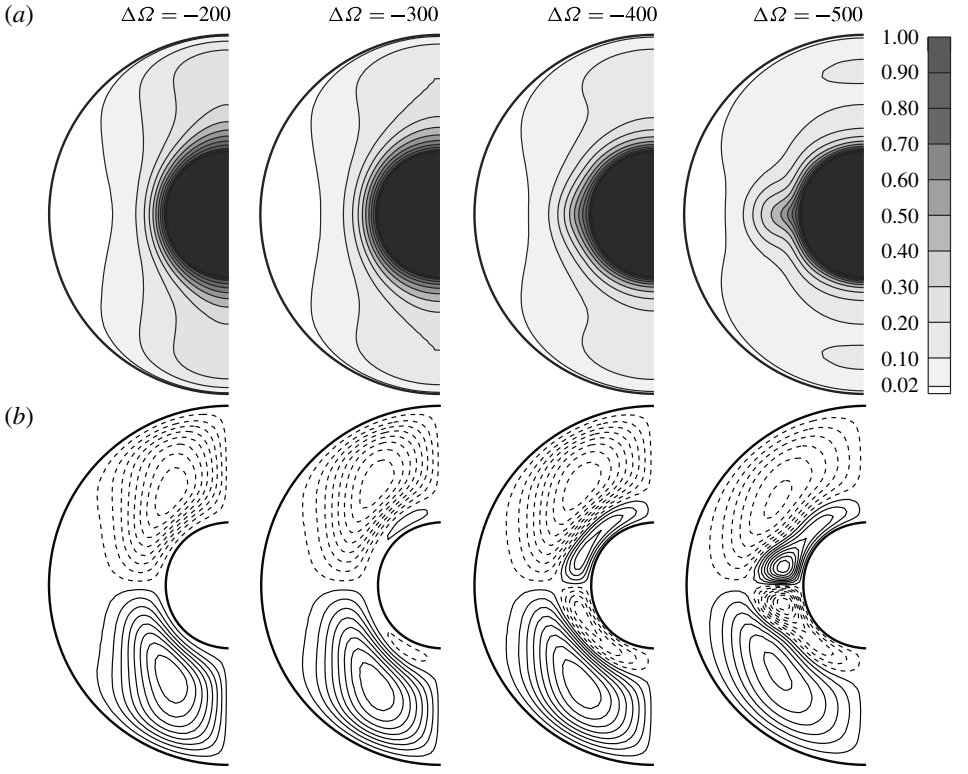


FIGURE 8. Axisymmetric flow for $\Omega = 10^2$ and $\Delta\Omega < 0$, developing a double-roll structure in the meridional circulation, (*b*), as $|Ro| = |\Delta\Omega|/\Omega$ is increase beyond 2. (*a*) The normalized angular velocity.

The first non-axisymmetric instability now clearly differs from the equatorial jet instability and sets in earlier, for example at $\Delta\Omega_c = -500$ for $\Omega = 10^2$. Figure 6(*b*) and figure 9(*a*) illustrate the structure of this new double-roll instability which has a pronounced wavy form around the equatorial plane with a dominant wavenumber $m = 2$. It is equatorially antisymmetric and, like all other primary instabilities, drifts in the direction of the differential rotation. Being linked to the inner roll pair, the instability resides deeper in the shell than the previously described solutions. The fact that the zonal jet has not developed to the same degree as in the equatorial jet instability also points towards a different mechanism.

As $\Delta\Omega$ is decreased further, the inner meridional cells extend outward while the outer cells become weaker and retreat to higher latitudes. An equatorial jet scenario very similar to the one found at slow outer boundary rotations develops once $|Ro| \gg 1$ and the Coriolis force loses its influence. The respective instability sets in at about $\Delta\Omega = -1560$, now with a wavenumber $m = 2$ instead of $m = 3$. Interaction with the $m = 2$ double-roll instability, that drifts about 15 % faster, once more leads to oscillation in the r.m.s. flow amplitude. At larger differential rotation rates, the latter instability dominates the dynamics, the oscillation ceases and the solution again drifts homogeneously (see the different regimes indicated in figure 7*b*).

When further decreasing $\Delta\Omega$ additional wavenumbers set in, the solution acquires equatorially symmetric contributions and it becomes chaotic. Figure 9(*c*) depicts the

https://doi.org/10.1017/jfm.2013.545 Published online by Cambridge University Press

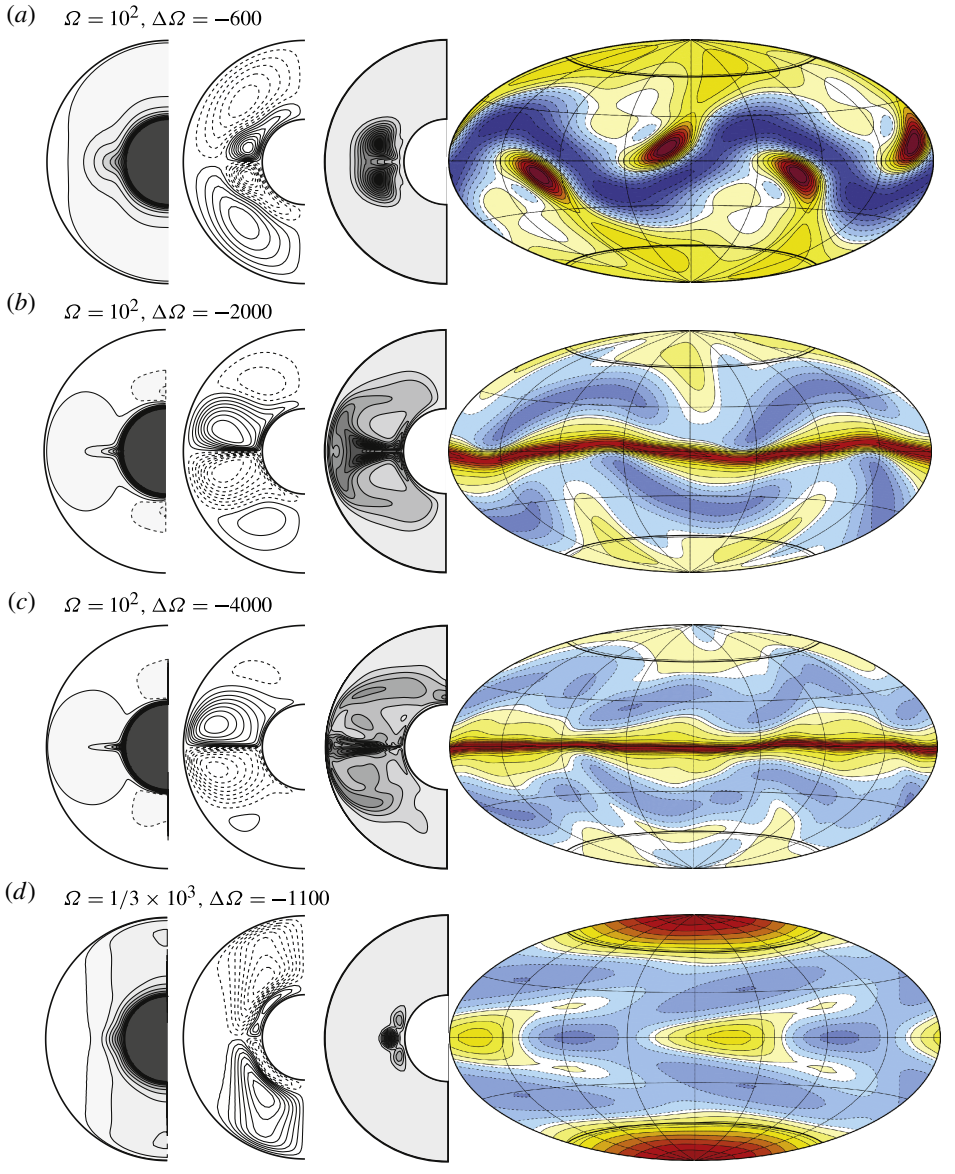


FIGURE 9. (Colour online) Visualization of the different $\Delta\Omega < 0$ solutions found in the intermediate-Ω regime. See figure 5 for more explanation.

slightly chaotic solution at $\Delta\Omega = -4000$. The drift and an interaction between the $m = 2$ instabilities and a new $m = 3$ mode clearly dominate the time dependence while the axisymmetric flow contributions vary only little in time. The snapshot shown in figure 9 very closely resembles the perfectly equatorially symmetric time-averaged axisymmetric flow.

The new equatorially antisymmetric double-roll instability is found for $\Omega = 50$ and $\Omega = 10^2$. At $\Omega = 2 \times 10^2$ and $\Omega = (1/3) \times 10^3$, the meridional circulation still features the double-roll structure but the first non-axisymmetric instability is now

https://doi.org/10.1017/jfm.2013.545 Published online by Cambridge University Press

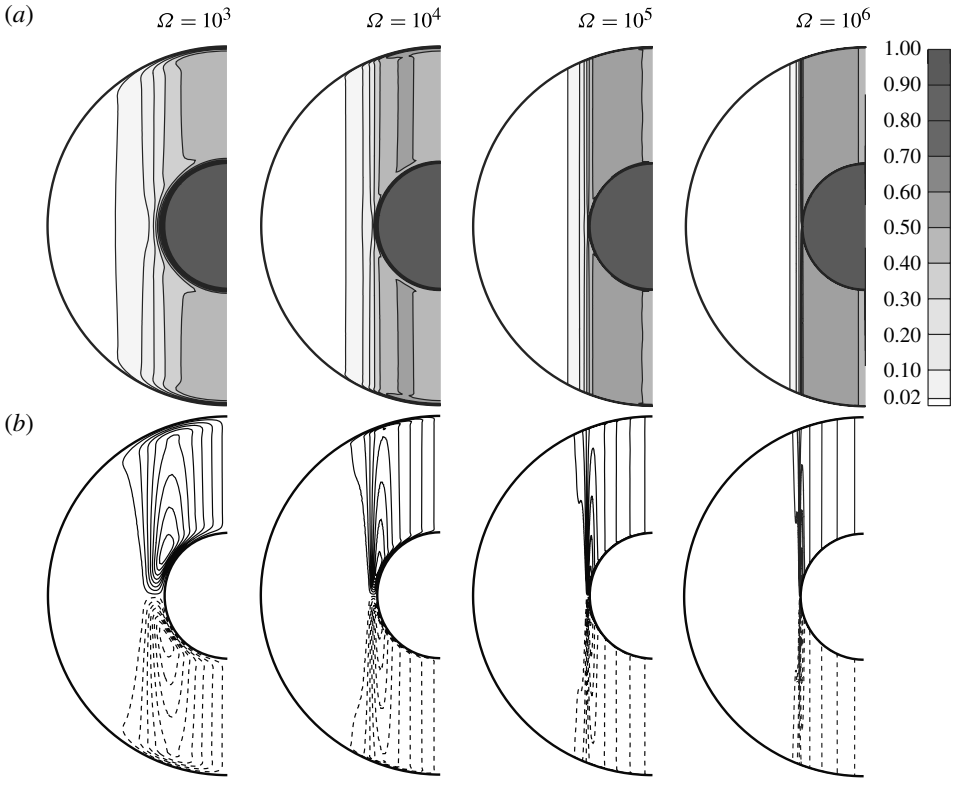


FIGURE 10. (*a*) Normalized axisymmetric zonal flow and (*b*) meridional circulation for $\Delta\Omega = 10^{-4}$ and different large outer boundary rotation rates.

equatorially symmetric. A likely cause is the growing influence of the Coriolis force which suppresses z-dependence and thus promotes equatorially symmetric flows. The increase in the critical differential rotation rate $\Delta\Omega_c$ illustrated in figure 1 is another consequence. Figure 9(*d*) depicts the solution close to onset at $\Omega = (1/3) \times 10^3$ and shows that this equatorially symmetric double-roll instability, being associated with the inner roll pair, also sits deep in the shell. At onset, the poloidal flow contribution is weaker than the toroidal at $U_P/U_T \approx 0.1$, but since the zonal jet has not yet developed the instability may nevertheless rely on the shear in the meridional circulation.

3.3. *Fast outer boundary rotation:* $\Omega \geqslant 10^3$

3.3.1. *Axisymmetric solution*

Figure 10 illustrates how the axisymmetric basic flow develops as Ω increases from 10^3 to 10^6. It becomes progressively geostrophic with minimal variation along the rotation axis and approaches a solution that has been described by Proudman (1956) and Stewartson (1966), relying on an asymptotic analysis for large $\Omega \gg 1$ and small $Ro \ll 1$,

They show that the tangent cylinder (TC) with cylindrical radius $s = r_i$ that is attached to the inner core equator forms an important dynamical boundary. Outside the TC the fluid predominantly sticks to the outer boundary so that the angular velocity $\bar{\omega}$ vanishes. Inside the TC the fluid mainly rotates with the intermediate rate $\bar{\omega} = (1/2)\Delta\Omega$ but asymptotically approaches $\Delta\Omega$ as s approaches r_i. Ekman

https://doi.org/10.1017/jfm.2013.545 Published online by Cambridge University Press

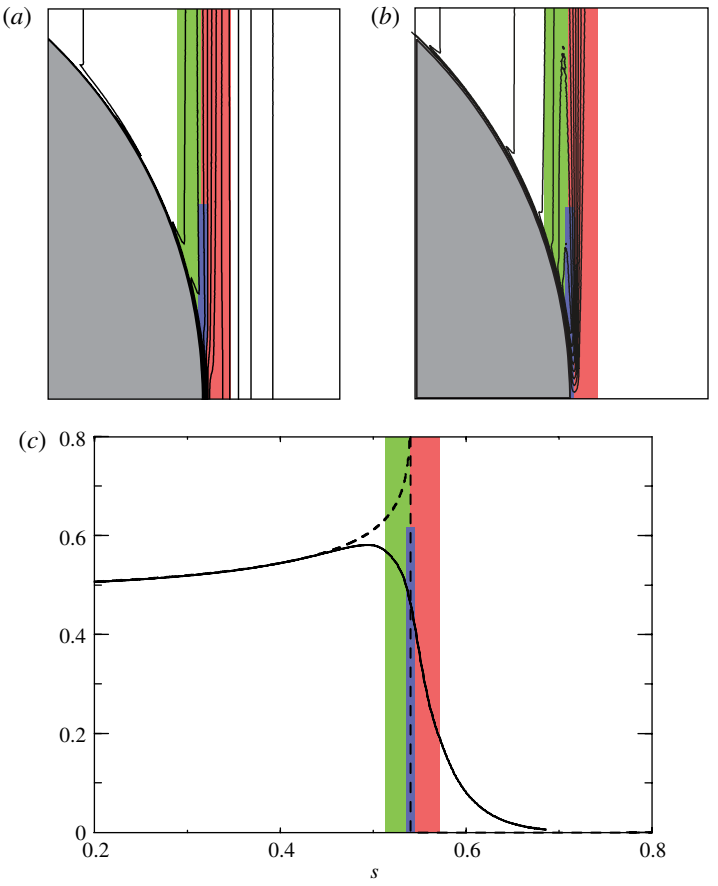


FIGURE 11. (Colour online) The three different components of the nested Stewartson layer illustrated with an axisymmetric numerical solution at $\Omega = 10^6$: (*a*) contour lines of the angular velocity; (*b*) the meridional circulation streamlines; (*c*) the angular velocity profile along with the asymptotic solution for infinite Ω (dashed line). See text for more explanation.

layers with a thickness proportional to $\Omega^{-1/2}$ serve to adjust the azimuthal flow inside the TC to the boundary rotations. The meridional circulation is predominantly concentrated in the region inside the TC where centrifugal forces drive motions away from the rotation axis in the Ekman layer attached to the faster rotating boundary and towards the rotation axis in the second Ekman layer. What was named Coriolis driving above is now restricted to the Ekman layers. The ratio of poloidal to toroidal flow amplitudes therefore scales like $U_P/U_T \sim \Omega^{-1/2}$. The direction of the zonal flow and the meridional circulation depend on the sign of $\Delta\Omega$.

A complex nested shear layer, commonly called the Stewartson layer, consolidates the motions inside and outside the tangent cylinder. Its different contributions are illustrated in figure 11. A layer attached to the outer side of the TC (red or medium grey) with thickness $\Omega^{-1/4}$ compensates the main jump in $\bar{\omega}$ and hosts the majority of a meridional circulation jet that connects the two Ekman layers. A second boundary layer (green or light grey) with thickness $\Omega^{-2/7}$ is attached to the inside of the TC and mainly serves to adjusts the first s-derivative of $\bar{\omega}$. An inner boundary layer (blue or

https://doi.org/10.1017/jfm.2013.545 Published online by Cambridge University Press

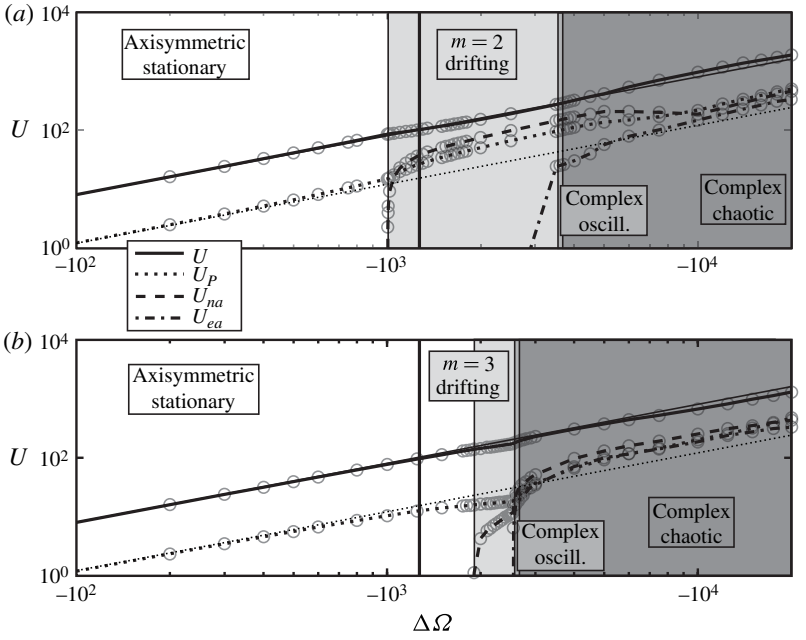


FIGURE 12. Dimensionless flow amplitudes (Reynolds numbers) for $\Omega = 10^3$ and (*a*) super-rotating or (*b*) sub-rotating inner boundary. Thick vertical lines mark the onset of the drifting non-axisymmetric instability for $\Omega \ll 1$. For more explanation see figure 2.

dark grey) centred around $s = r_i$ with thickness $\Omega^{-1/3}$ adjusts the radial flow and the second s-derivative of $\bar{\omega}$. The thickness of the Ekman layer increases to $\Omega^{-2/5}$ around the inner core equator.

A more detailed comparison of numerical solutions with the asymptotic solution can be found in Dormy *et al.* (1998) who point out that the complex nested structure of the Stewartson layer only begins to show beyond $\Omega = 10^5$.

3.3.2. *Non-axisymmetric solutions*

For super-rotation the first non-axisymmetric instability becomes equatorially symmetric and assumes a predominantly geostrophic configuration for $\Omega = (1/3) \times 10^3$. This value also marks the start of a power-law dependence of $\Delta\Omega_c$ on Ω. In the sub-rotation case the double-roll instability still prevails at $\Omega = (1/3) \times 10^3$ and a new helical instability is found at $\Omega = 10^3$. Nearly geostrophic instabilities then rule for $\Omega \geqslant (1/3) \times 10^4$. A more precise definition of the fast Ω regime is thus $\Omega \geqslant (1/3) \times 10^3$ for super-rotation but $\Omega \geqslant (1/3) \times 10^4$ for sub-rotation. The different regime boundaries can be explained by the fact that the differential rotation reinforces Ω for super-rotation and diminishes it for sub-rotation. For sub-rotation the critical rotation rate only seems to follow a power law similar to that in the super-rotation case once $\Omega \geqslant 3 \times 10^5$. The dependence of $\Delta\Omega$ on Ω is discussed in more detail in § 3.3.3.

Figure 12 shows the regime diagram for $\Omega = 10^3$; figures 13, 14 and 15 illustrate the different solutions encountered as $|\Delta\Omega|$ is increased to 10^4 for super- and sub-rotation, respectively. Below the onset of the first non-axisymmetric instability, sub-rotation and super-rotation cases differ only in flow direction and remain identical to the Stewartson-type solution in structure. The critical differential rotation rates

https://doi.org/10.1017/jfm.2013.545 Published online by Cambridge University Press

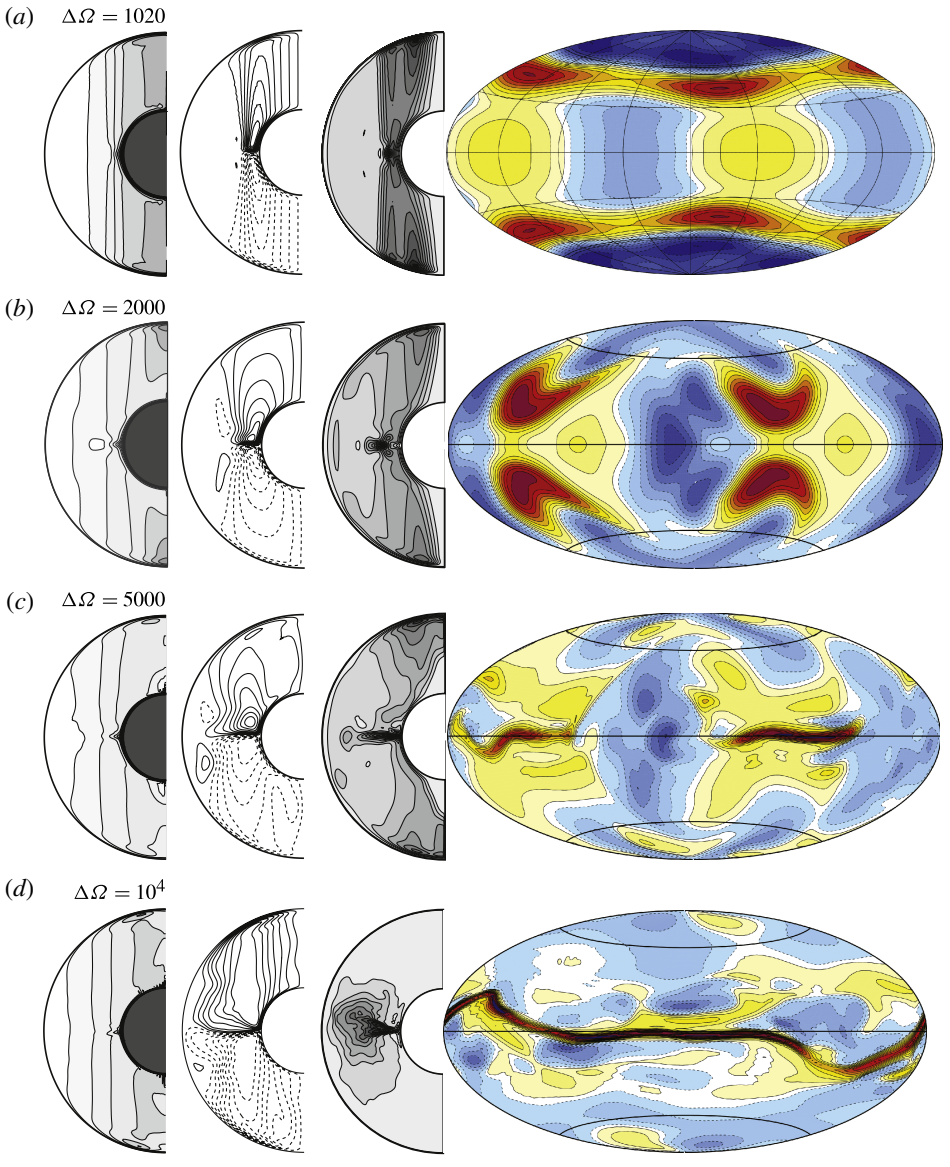


FIGURE 13. (Colour online) Illustration of the different solutions for $\Omega = 10^3$ and $\Delta\Omega > 0$: (*a,b*) the flow close to onset of the first non-axisymmetric instability and in a more developed state; (*c,d*) more complex solutions with a chaotic time dependence. Left to right: normalized angular velocity, meridional circulation, azimuthally averaged non-axisymmetric kinetic energy and radial flow in mid depth in the shell. See figure 5 for more explanation.

are $\Delta\Omega_c = 1006$ and $\Delta\Omega_c = -1900$ with critical wavenumbers $m_c = 2$ and $m_c = 3$, respectively. Both instabilities are equatorially symmetric and once more drift in the direction of $\Delta\Omega$. The higher absolute differential rotation required for sub-rotation is typical for the Stewartson layer instabilities (Hollerbach 2003).

The three-dimensional rendering in figure 15 demonstrates that both instabilities are connected to the Stewartson layer but only the super-rotation instability shows

https://doi.org/10.1017/jfm.2013.545 Published online by Cambridge University Press

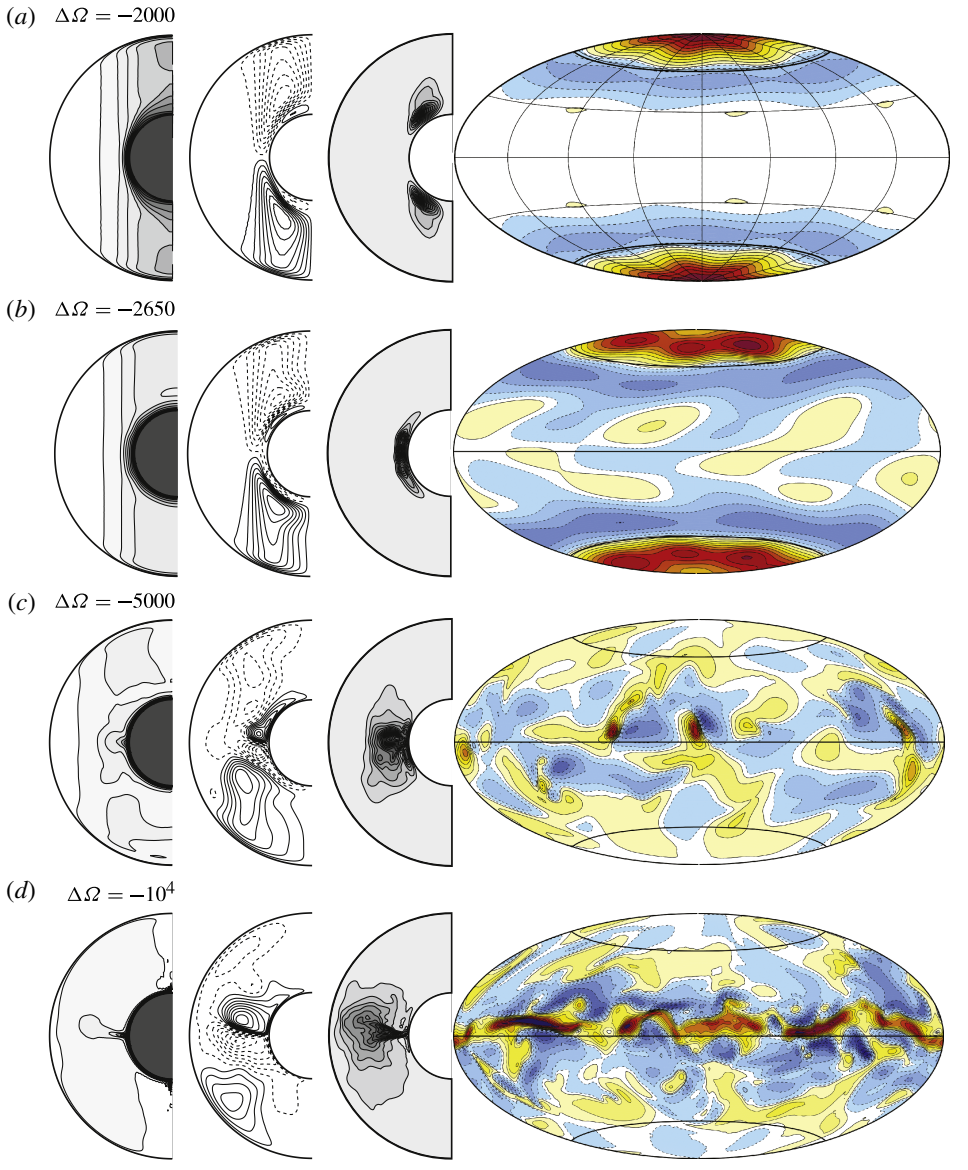


FIGURE 14. (Colour online) Illustration of the different solutions for $\Omega = 10^3$ and $\Delta\Omega < 0$. See figure 5 for more explanation.

the nearly geostrophic shape typical for larger Ω values while the sub-rotation instability is characterized by a strongly z-dependent helical structure. This new type of instability occupies only a small fraction of the Ω parameter space between the double-roll regime at $\Omega = (1/3) \times 10^3$ and nearly geostrophic instabilities for $\Omega \geqslant (1/3) \times 10^4$. The super-rotation instability occupies the region just outside and inside the tangent cylinder while the helical instability remains confined to the region inside the tangent cylinder. This is typical for Stewartson layer instabilities at large but not too large values of Ω (Hollerbach 2003; Schaeffer & Cardin 2005).

https://doi.org/10.1017/jfm.2013.545 Published online by Cambridge University Press

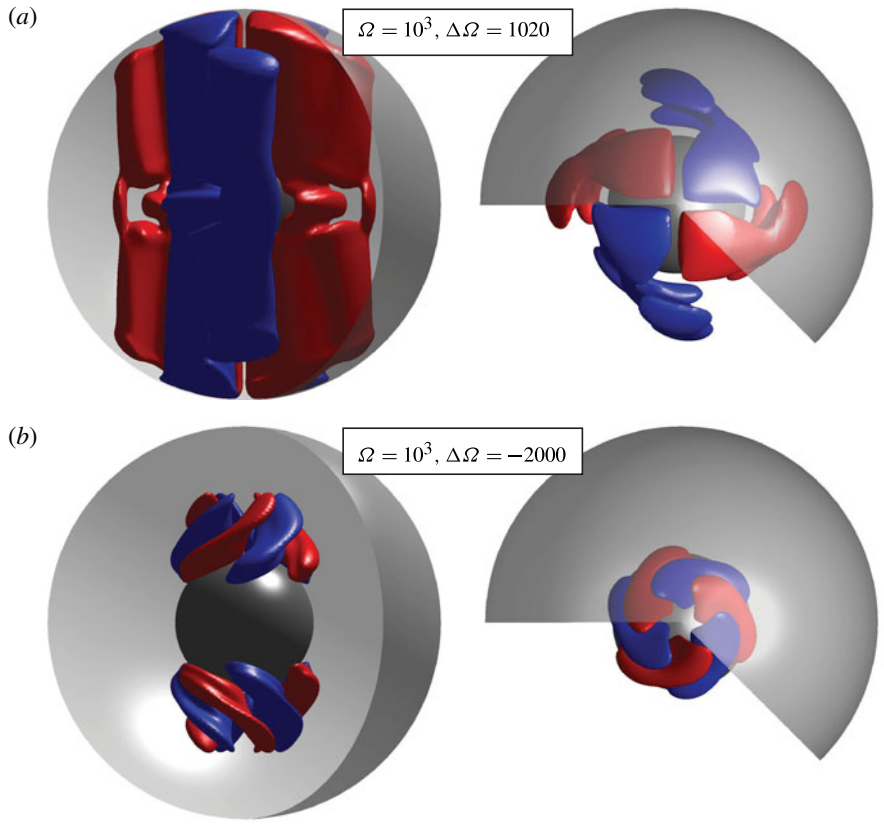


FIGURE 15. (Colour online) Isosurfaces of the non-axisymmetric flow away from (red online) and towards (blue online) the rotation axis (U_s). Depicted are cases close to onset of (*a*) the super-rotation and (*b*) sub-rotation instability at $\Omega = 10^{-3}$.

As $\Delta\Omega$ is increased in the super-rotation case, the focus of the instability gradually moves from latitudes around the tangent cylinder to the equator (see figure 13) as the evolving equatorial jet promotes a gradual transition to the equatorially symmetric instability. This is clearly illustrated in the third column of figure 13 which shows the azimuthally averaged kinetic energy of the non-axisymmetric flow components to illustrate the focus of the instabilities. Around $\Delta\Omega = 3500$ a wavenumber $m = 1$ instability sets in and causes a fast but weak oscillation in the r.m.s. flow amplitude. As in other cases, these oscillations are likely to be caused by a nonlinear interaction of the two modes. The $m = 1$ instability is too weak to clearly determine its properties but since its appearance coincides with the growth of equatorially antisymmetric flow components it is likely to have this symmetry (see figure 12).

Nonlinear interactions between the $m = 1$ and $m = 2$ instabilities quickly lead to the excitation of a full wavenumber spectrum and a chaotic time dependence. At $\Delta\Omega = 10^4$ or $Ro = 10$ the antisymmetric equatorial jet instability starts to play a significant role. Figure 13(*d*) demonstrates that the equatorial jet undulates strongly in latitude, indicating significant equatorially antisymmetric flow components. Figure 12 shows that this goes along with a decrease of poloidal and non-axisymmetric flow contributions.

https://doi.org/10.1017/jfm.2013.545 Published online by Cambridge University Press

For sub-rotation and close to onset the $m_c = 3$ instability is confined inside the tangent cylinder as is illustrated in figure 14. A second non-axisymmetric instability with wavenumber $m = 2$ sets in around $\Delta\Omega = -2575$. A clearer separation of the two modes at $\Delta\Omega = -2650$ allows the determination that the $m = 2$ instability drifts about 45 % slower than the $m = 3$ instability. Once more, nonlinear interaction between the two modes excites other harmonics and leads to an oscillation of the r.m.s. flow amplitude with a frequency of $\omega_f = 320$. Being associated with the emergence of the inner roll pair evident in figure 14(*b*), the second instability is of the equatorially antisymmetric deep-seated double-roll type described above. Figure 14(*b*) clearly demonstrates that the non-axisymmetric kinetic energy is predominantly associated with the inner roll pair.

When further increasing $\Delta\Omega$, the equatorial jet instability is expected to take over once $|Ro| \gg 1$. Figures 13(*d*) and 14(*d*) indeed start to show similar features at $Ro = 10$ and $Ro = -10$, in particular the dominance of the outward directed wavy radial jet around the equator. The evolution of the kinetic energy focus, shown in the third column of figures 13 and 14, confirms this trend. The super-rotation case remains more geostrophic so that the Coriolis force still seems to play a significant role. This may also be the reason for the less developed zonal equatorial jet and the larger length scales. In the sub-rotation case the inner roll pair is still confined to lower latitudes so that the meridional circulation pattern differs significantly from that in the super-rotation simulation. However, these remaining differences are expected to vanish at yet higher absolute Rossby numbers.

The drift remains a prominent time dependence of the non-axisymmetric features at $\Delta\Omega = 10^4$ and $\Delta\Omega = -10^{-4}$ but more complex time variations are also important. In particular the smaller-scale structures in the equatorial region and the undulation of the equatorial jet vary significantly. In the super-rotation case, the axisymmetric flow components, illustrated in first two panels of figure 13(*d*), remain largely geostrophic over time. The meridional circulation is sometimes stronger in the northern and sometimes in the southern hemisphere which leads to deviations in the equatorial jet direction. In addition to the jet direction the complex angular velocity structures inside the tangent cylinder also vary considerably. Time averages of the axisymmetric flow are perfectly equatorially symmetric, however, and generally similar to the illustration shown in figure 13. The behaviour of the sub-rotation simulation is similar but the variations are more pronounced. The secondary high-latitude meridional circulation roll, visible in the southern hemisphere in figure 14(*d*), strongly oscillates in amplitude. At some times it is more prominent in the northern, at other times in the southern hemisphere. Time-averaged axisymmetric flows are once more perfectly equatorially symmetric and show a high-latitude roll pair with about half the amplitude of the low-latitude pair.

Figure 16 provides a regime overview for $\Omega = 10^4$ while figures 17 and 18 show typical solutions and figure 19 is an attempt to visualize their three-dimensional structure. The super-rotation case becomes unstable at $\Delta\Omega_c = 2010$ where an $m_c = 4$ solution sets in. For sub-rotation the first non-axisymmetric instability has the wavenumber $m_c = 1$ and sets in at $\Delta\Omega_c = -3790$. This agrees well with the results reported by Hollerbach (2003).

Like at $\Omega = 10^3$ super- and sub-rotation instabilities are located around and in the tangent cylinder, the former predominantly outside and the latter more inside this imaginary boundary. Contrary to the solutions found at $\Omega = 10^3$ both instabilities are now largely geostrophic as is clearly illustrated by figure 19. As the differential rotation is increased, the super-rotation instability spreads inside the tangent cylinder

https://doi.org/10.1017/jfm.2013.545 Published online by Cambridge University Press

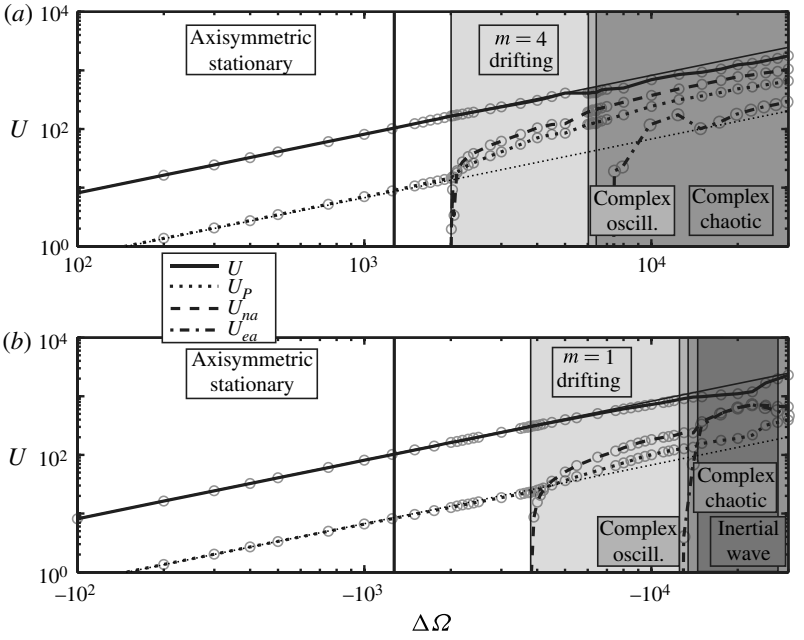


FIGURE 16. Dimensionless flow amplitudes (Reynolds numbers) for $\Omega = 10^4$ and (*a*) super-rotating or (*b*) sub-rotating inner boundary. Thick vertical lines mark the onset of the drifting non-axisymmetric instability for $\Omega \ll 1$. For more explanation see figure 2.

but also tends to fill the whole shell while the equatorial jet develops. The sub-rotation instability remains more confined to the region inside the tangent cylinder until the equatorial jet clearly develops at higher differential rotation rates.

Close to onset, both cases show the drifting behaviour that will be discussed further in § 3.4. For $\Delta\Omega > 0$ an equatorially symmetric wavenumber $m = 3$ instability starts to dominate the solution at $\Delta\Omega = 6010$ while the $m = 4$ instability takes a background role (see figure 17*b*). The $m = 3$ instability drifts about 15 % faster than the $m = 4$ mode (see table 2). Interaction between the two once more leads oscillatory and then chaotic time behaviour.

As already observed for $\Omega = 10^3$, the focus of the instability gradually moves to lower latitudes as $\Delta\Omega$ is increased and the role of the equatorial jet grows. At $\Delta\Omega = 10^4$ equatorially antisymmetric components become more important as is evident from the regime diagram 16 and from the radial flow shown in the fourth column of figure 17. Around $\Delta\Omega = 3 \times 10^4$, however, the relative importance of the antisymmetric flow contributions starts to decrease. Figure 17 illustrates that low-latitude flows play an important role so that an equatorial jet instability may be responsible. However, the complex nature of the solution complicates a clear separation of different instabilities and the available computer resources did not allow higher *Ro* values to be reached, where the equatorial jet instabilities are likely to dominate.

The drift remains the predominant time dependence of non-axisymmetric features in the $\Delta\Omega = 3 \times 10^4$ solution illustrated in figure 17(*d*). Smaller-scale features show a more pronounced additional time dependence. The equatorial jet and an otherwise largely geostrophic and equatorially symmetric configuration are persistent features

https://doi.org/10.1017/jfm.2013.545 Published online by Cambridge University Press

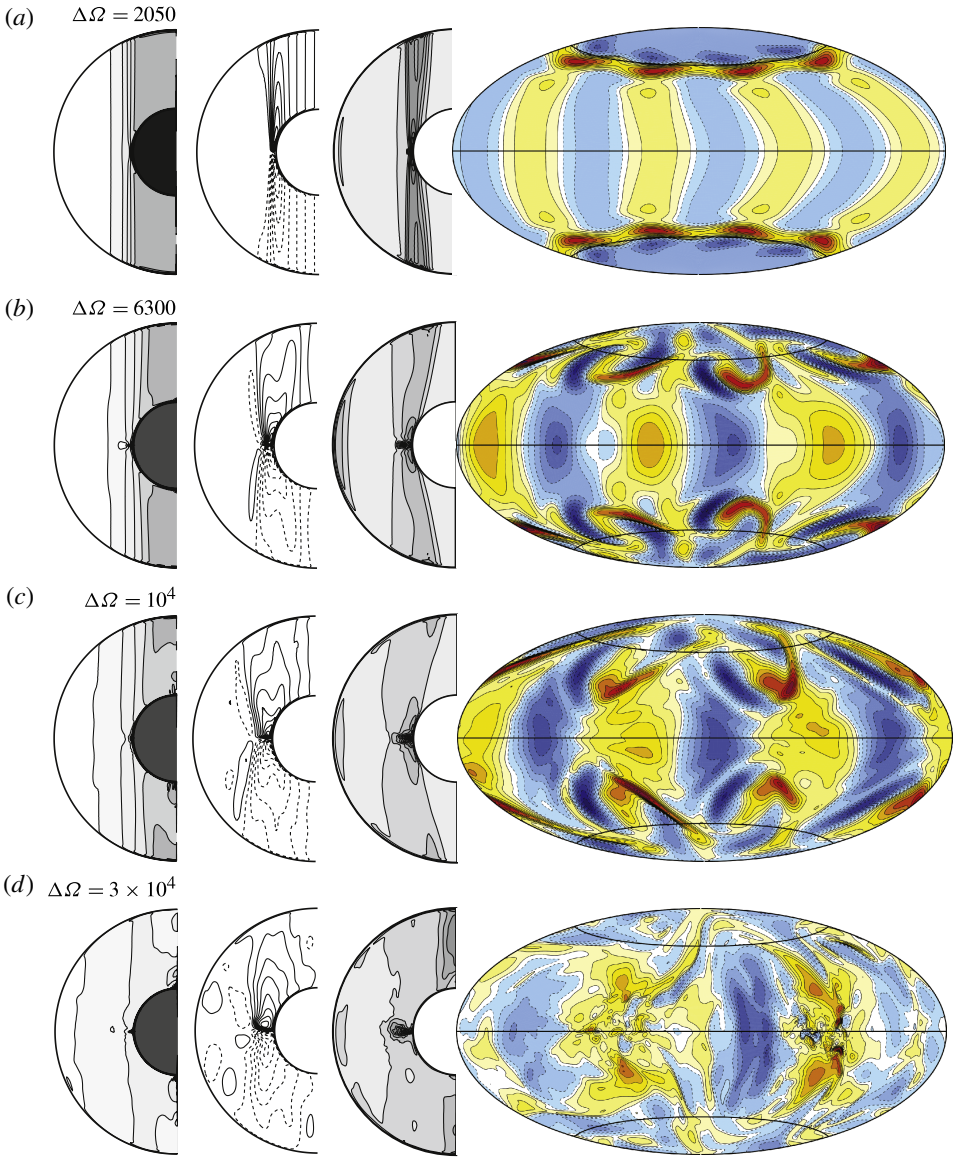


FIGURE 17. (Colour online) Illustration of the different solutions for $\Omega = 10^4$ and $\Delta\Omega > 0$: (*a,b*) the flow close to onset of the first non-axisymmetric instability and in a more developed state; (*c,d*) more complex solutions with a chaotic time dependence. Left to right: normalized angular velocity, meridional circulation, azimuthally averaged non-axisymmetric kinetic energy and radial flow in mid depth in the shell. See figure 5 for more explanation.

in the axisymmetric flow components illustrated in figure 17(*d*). The weaker small-scale details further away and very close to the rotation axis show a stronger time dependence but average out over time.

For $\Delta\Omega < 0$ a full wavenumber spectrum is quickly excited as $|\Delta\Omega|$ is increased beyond its critical value. The $m = 1$ mode remains clearly dominant, however, and outside the tangent cylinder the solution starts to concentrate in a narrower longitude

https://doi.org/10.1017/jfm.2013.545 Published online by Cambridge University Press

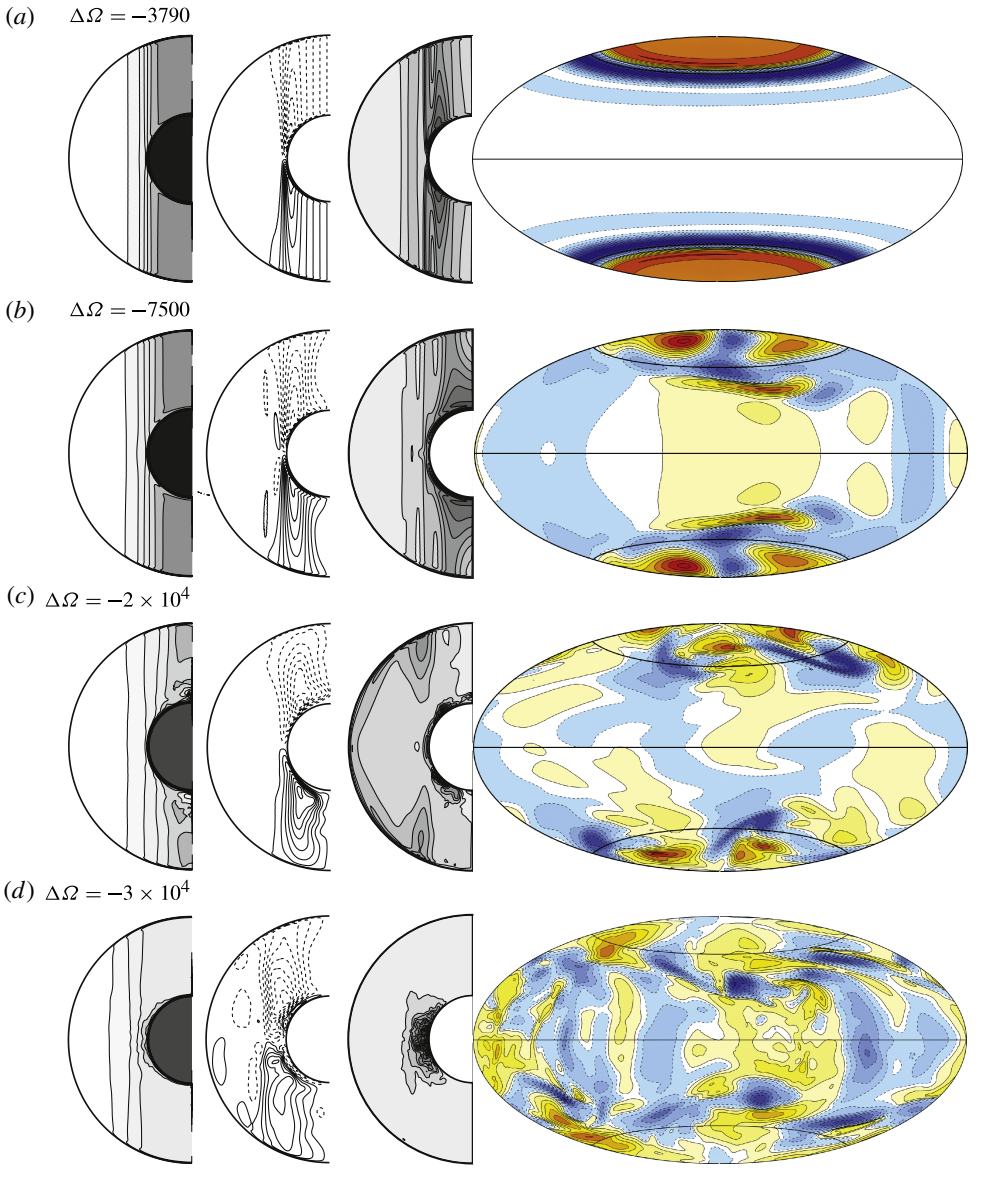


FIGURE 18. (Colour online) Illustration of the different solutions for $\Omega = 10^4$ and $\Delta\Omega < 0$. See figure 5 for more explanation.

band (see figure 18*b*). A second instability sets in around $\Delta\Omega = -1.3 \times 10^4$ and once more causes an oscillatory behaviour. On increasing $|\Delta\Omega|$ further, this new instability grows in amplitude and clearly dominates the solutions at $\Delta\Omega = -2 \times 10^4$, accounting for 97 % of the non-axisymmetric r.m.s. flow amplitude. The non-axisymmetric flow structure illustrated in figure 19(*c*) and the drift frequency allowed this instability to be identified as an equatorially antisymmetric fast inertial mode with wavenumber $m = 2$. A temporal Fourier analysis of the individual wavenumber contributions also revealed

https://doi.org/10.1017/jfm.2013.545 Published online by Cambridge University Press

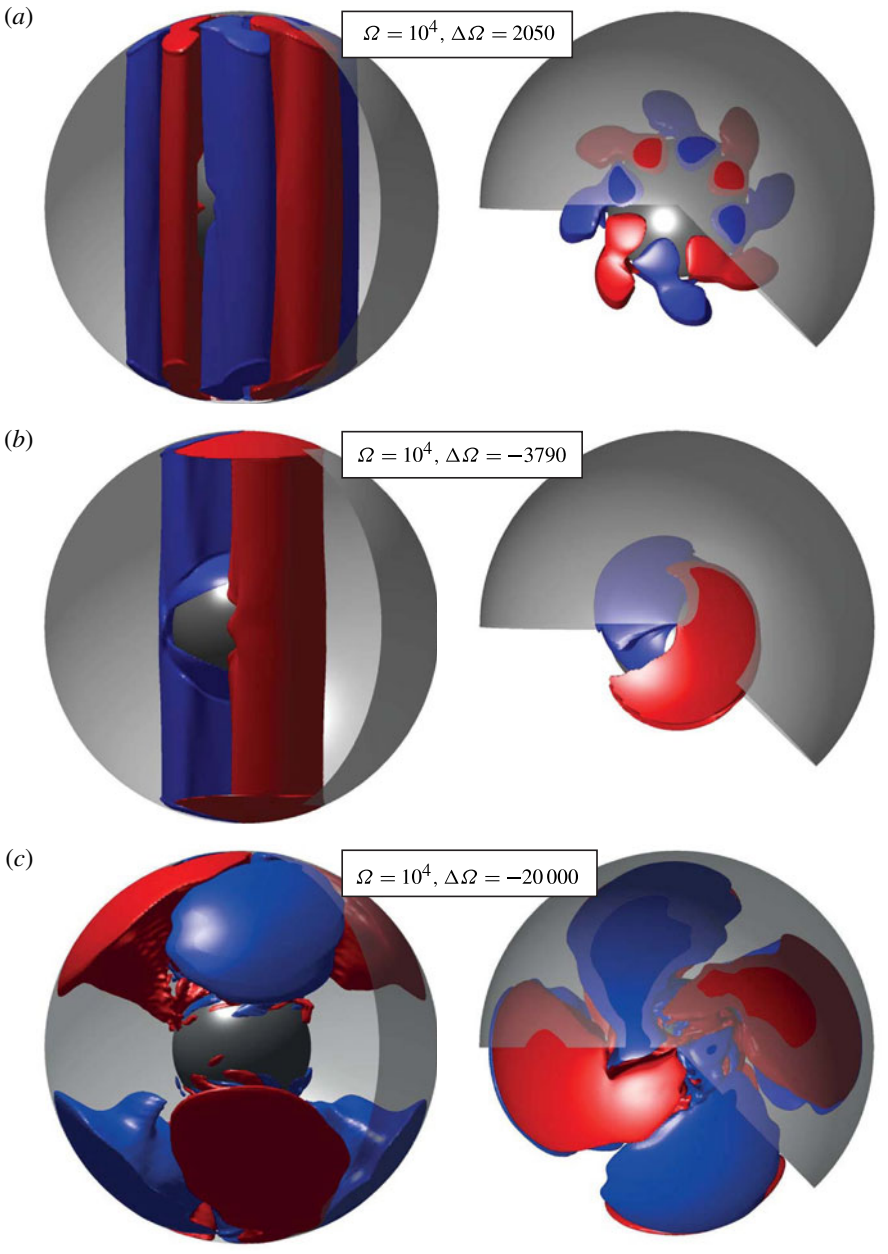


FIGURE 19. (Colour online) Isosurfaces of the non-axisymmetric flow away from (red online) and towards (blue online) the rotation axis (U_s). Depicted are cases close to onset of (*a*) the super-rotation and (*b*) sub-rotation instability at $\Omega = 10^{-4}$. (*c*) The fast equatorially antisymmetric inertial mode encountered for sub-rotation at $\Omega = 10^{-4}$.

a second weaker equatorially antisymmetric fast inertial mode with $m = 1$. Inertial waves are further discussed in § 3.4.

For differential rotations below $\Delta\Omega = -2 \times 10^4$ the relative importance of the inertial modes gradually decreases. Figure 18(*d*) illustrates that the equatorially

https://doi.org/10.1017/jfm.2013.545 Published online by Cambridge University Press

Ω	$\Delta\Omega$	m	instab.	ω_d	$\omega_d/\Delta\Omega$	σ_{SC}	N	n	σ	Mode
0	1270	3	EJ, EA	93	0.073					
	1500	3	EJ, EA	104	0.069					
	2100	3	EJ, EA	150	0.071					
		1	EJ, ES	120	0.057					
10^2	-600	2	DR, EA	-95	0.158	0.95				
	-2000	2	EJ, EA	-75	0.045	0.75				
10^3	1006	2	SL, geo.	123	0.122	-0.123	1	2	-0.1160	geo.
	-1900	3	SL, hel.	-874	0.460	1.31				
	-2575	3	SL, hel.	-1033	0.401	1.55				
		2	DR, EA	-1495	0.580	1.50				
10^4	2010	4	SL, geo.	397	0.198	-0.0794	2	4	-0.0656	geo.
	2050	4	SL, geo.	402	0.196	-0.0804	2	4	-0.0656	geo.
	6300	4	SL, geo.	698	0.111	-0.1396	2	4	-0.0656	geo.
		3	SL, geo.	8 10	0.129	-0.1215	1	2	-0.1266	geo.
	-3790	1	SL, geo.	-861	0.227	0.0431	2	4	-0.0341	geo.
	-3900	1	SL, geo.	-879	0.225	0.0440	2	4	-0.0341	geo.
10^5	4500	8	SL, geo.	1111	0.247	-0.0444	3	6	-0.0484	geo.
	$-13\,300$	2	SL, geo.	-4968	0.374	0.0497	2	4	-0.0509	geo.
10^6	11 000	17	SL, geo.	3237	0.294	-0.0275	6	12	-0.0255	geo.
	$-32\,400$	16	SL, geo.	-9637	0.297	0.0771	2	4	-0.0700	geo.
10^4	$-20\,000$	2	SL, EA	-3600	0.180	0.360	0	1	0.3333	EA
		1	SL, EA	-6200	0.310	0.310	1	3	0.3060	EA
10^5	-10^5	2	SL, EA	-3.77×10^4	0.377	0.377	0	1	0.3333	EA
		1	SL, EA	-6.41×10^4	0.641	0.321	1	3	0.3060	EA

TABLE 2. Drifting instabilities in the spherical Couette system (columns 1–7) and inertial modes with the closest absolute frequency (columns 8–11). Column 4 characterizes the type of instability (EJ = equatorial jet, DR = double roll, SL = Stewartson layer) and its geometry (EA = equatorially antisymmetric, geo. = nearly geostrophic, hel. = helical). Column 7 lists the frequency σ_{SC} that results from the drift ω_d. This should be compared with the frequency of inertial modes given in column 10. The last column characterizes the geometry of the inertial modes. The last four lines list the equatorially antisymmetric fast inertial modes that have been identified in a spherical Couette experiment (Kelley *et al.* 2007; Rieutord *et al.* 2012).

symmetric flows at low to mid latitudes become more important at $\Delta\Omega = -3 \times 10^4$. The solution already bears some similarity to the super-rotation case at $\Delta\Omega = 3 \times 10^4$ (see figure 17*d*). A double-roll structure starts to appear but the inner pair still seems too weak to significantly influence the solution.

Again, the azimuthal drift remains the dominant time dependence of non-axisymmetric flow components with additional variations in the structural details. Axisymmetric flow components vary little over time so that figure 18(*d*) depicts a typical configuration. The time-averaged flow is once more perfectly equatorially symmetric, however, and features a third meridional circulation roll pair at about mid depth in the shell.

Figure 20 shows the regime diagram at $\Omega = 10^5$ which is broadly similar to that at $\Omega = 10^4$ in the sense that the same types of solutions are encountered, including inertial modes. However, there is a more pronounced cascade to lower wavenumbers. The first non-axisymmetric super-rotation instability sets in at $\Delta\Omega_c = 4500$ with a wavenumber of $m_c = 8$. As $\Delta\Omega$ is increased, pure drifting solutions with lower

https://doi.org/10.1017/jfm.2013.545 Published online by Cambridge University Press

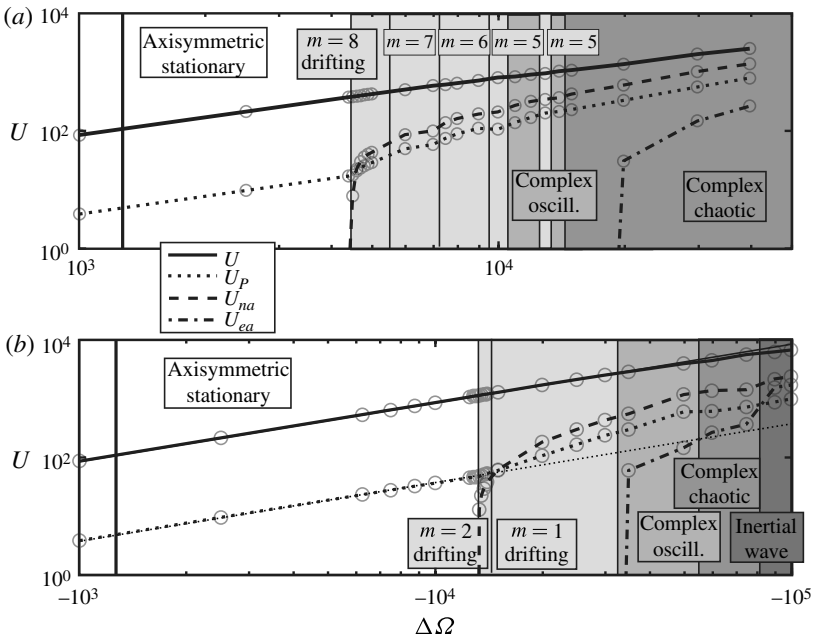


FIGURE 20. Dimensionless flow amplitudes (Reynolds numbers) for $\Omega = 10^5$ and (*a*) super-rotating or (*b*) sub-rotating inner boundary. Thick vertical lines mark the onset of the drifting non-axisymmetric instability for $\Omega \ll 1$. For more explanation see figure 2.

wavenumbers are found, for example $m = 7$ at $\Delta\Omega = 6000$, $m = 6$ at $\Delta\Omega = 8000$ and $m = 5$ at $\Delta\Omega = 10 \times 10^3$ (see figure 20).

Hollerbach *et al.* (2006) observe similar switches to lower wavenumbers in their numerical simulations and spherical Couette experiments at larger aspect ratio. They also report a hysteretic behaviour where the smaller wavenumbers would prevail at lower $\Delta\Omega$ values when gradually decreasing rather than increasing $\Delta\Omega$. The simulations presented here generally start with a full spectrum, typically using a larger $\Delta\Omega$ solution as initial condition. A few trial runs starting from solutions at lower $\Delta\Omega$ seem to confirm the hysteretic behaviour.

In addition to the cascade there is also a complex evolution of the time behaviour at $\Omega = 10^5$ (see figure 20). At $\Delta\Omega = 11\,000$ and $\Delta\Omega = 12\,000$ a secondary $m = 2$ mode interacts with the primary $m = 5$ mode which leads to oscillatory behaviour and the excitation of other modes. At $\Delta\Omega = 13\,000$, however, the $m = 2$ mode has ceased and a pure $m = 5$ drifting solution is found. At $\Delta\Omega = 14\,000$ an additional $m = 4$ mode sets in, leading to oscillatory and finally chaotic behaviour. The $m = 4$ mode still dominates at $\Delta\Omega = 2 \times 10^4$ but in the presence of a full background mode spectrum.

For sub-rotation the first instability sets in at $\Delta\Omega_c = -1.33 \times 10^4$ with $m_c = 2$. A mode switch to an $m = 1$ instability happens at $\Delta\Omega = -1.5 \times 10^5$. At $\Delta\Omega = -3.5 \times 10^4$ an additional equatorially antisymmetric instability sets in, leading to first oscillatory and then chaotic behaviour. Since this instability is rather weak at first, it is hard to single out and analyse. At $\Delta\Omega = -9 \times 10^4$, however, the two equatorially antisymmetric fast inertial modes already described above appear and account for 71 % of the non-axisymmetric r.m.s. flow amplitude. Their drift rates are somewhat larger than at $\Omega = 10^4$ (see table 2 above). At this larger Ω value the computer resources did

https://doi.org/10.1017/jfm.2013.545 Published online by Cambridge University Press

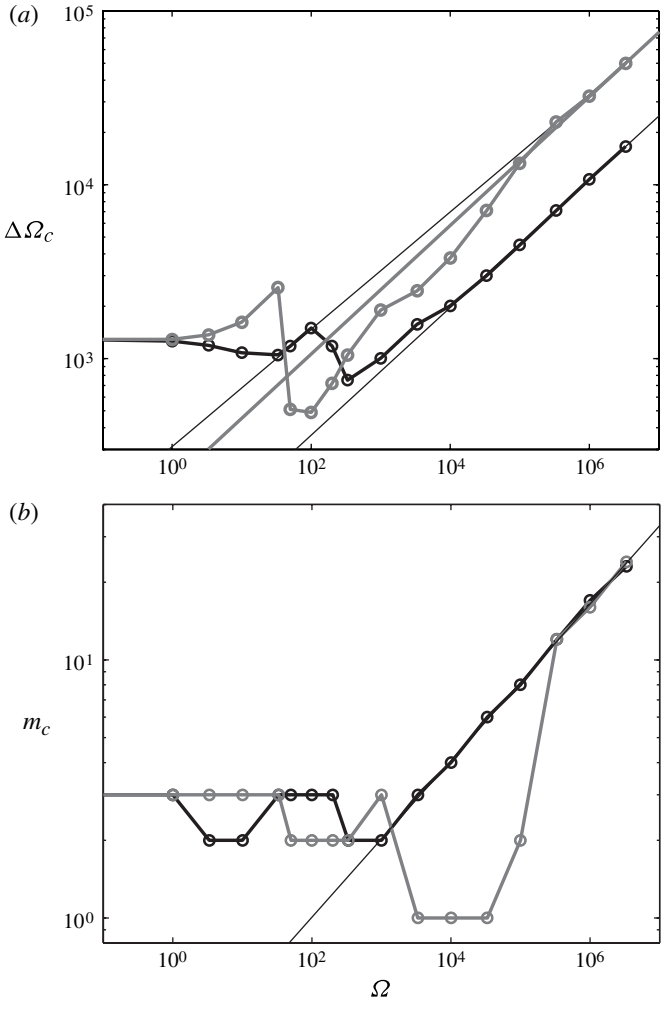


FIGURE 21. (*a*) Critical differential rotation and (*b*) wavenumber of the first non-axisymmetric instability for super-rotation (black lines and symbols) and sub-rotation (grey lines and symbols). In (*a*) the thin black lines represent the $\Omega^{0.37}$ scaling suggested by a least-square fit to the super-rotation values for $\Omega \geqslant 10^4$. The thin grey line represents the $\Omega^{0.34}$ scaling from a fit to the last three sub-rotation data points. For m_c both differential rotation directions imply a $\Omega^{0.30}$ scaling (thin black line).

not allow going beyond $|Ro| = 1$ in order to check whether the equatorial jet instability may once more take over.

3.3.3. *Very large Ω and scaling*

For $\Omega \geqslant (1/3) \times 10^6$ only the onset of the first non-axisymmetric instabilities has been determined in order to establish how $\Delta\Omega_c$ and m_c evolve in the large-Ω regime. Figure 21 demonstrates that for super-rotation the power laws $\Delta\Omega_c \approx 76\Omega^{0.37}$ and $m_c \approx 0.25\Omega^{0.30}$ nicely characterize the regime. The prefactors and exponents are based on linear least-square fits to $\ln(\Delta\Omega_c)$ and $\ln(m_c)$ for $\Omega \geqslant 10^4$.

https://doi.org/10.1017/jfm.2013.545 Published online by Cambridge University Press

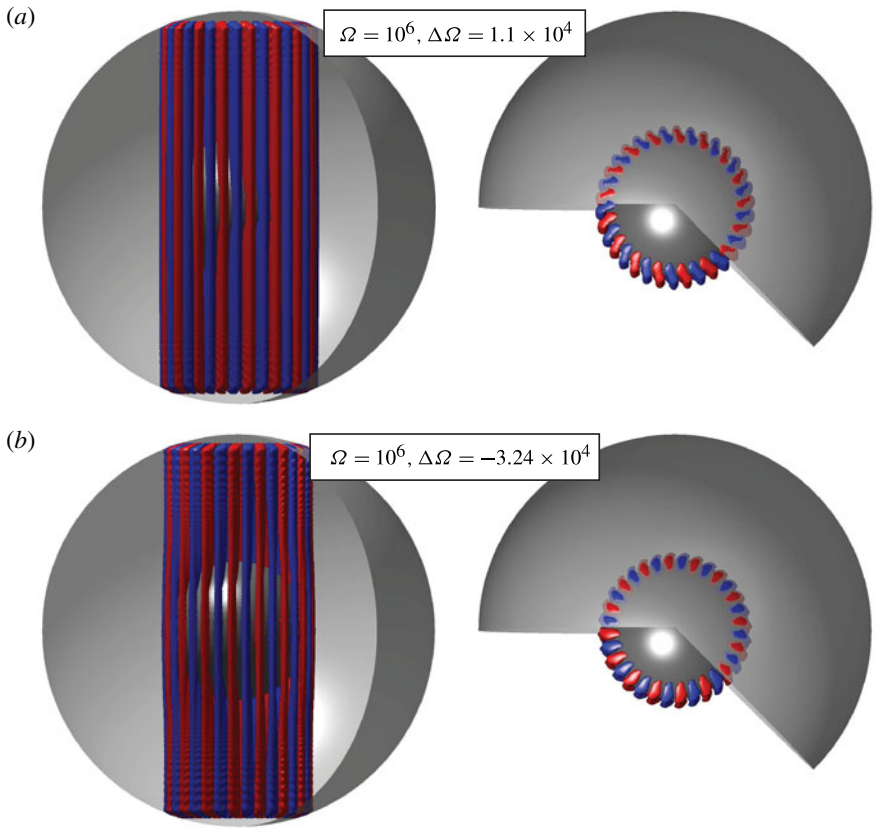


FIGURE 22. (Colour online) Isosurfaces of the non-axisymmetric flow away from (red online) and towards (blue online) the rotation axis (U_s). Depicted are cases close to onset of (*a*) the super-rotation and (*b*) sub-rotation instability at $\Omega = 10^6$.

For sub-rotation clear power laws can only be established for $\Omega \geqslant (1/3) \times 10^6$ and yield $\Delta\Omega_c \approx 311\Omega^{0.34}$ and $m_c \approx 0.25\Omega^{0.30}$. The prefactors and exponents are now only based on the three largest Ω values which may explain the different exponents in the $\Delta\Omega_c$ scaling for super- and sub-rotation. The scaling for the critical wavenumber is identical to that for super-rotation.

Figure 22 compares the super- and sub-rotation instabilities for $\Omega = 10^6$ and demonstrates that they not only follow a similar scaling but also have a very similar structure. The axisymmetric flow components remain identical to the ones depicted in figures 10 and 11 in both cases. Moreover, both instabilities now have a very similar energy focus around the tangent cylinder as is demonstrated by figure 23. An outer boundary rotation rate of $\Omega = (1/3) \times 10^6$ thus seems to mark the transition from the low-wavenumber Stewartson layer instability particular to sub-rotation to larger-wavenumber instabilities that also characterize super-rotation cases. The differences in the absolute values of $\Delta\Omega_c$ and in the drift remain, however. Super-rotation instabilities always drift prograde while the sub-rotation instabilities drift retrograde.

Hollerbach (2003) examines the linear onset between $\Omega = 10^{0.35}$ and $\Omega = 10^5$ and reports $\Delta\Omega_c \sim \Omega^{0.35}$ for super-rotation and $\Delta\Omega_c \sim \Omega^{0.55}$ for sub-rotation. The former scaling exponent agrees reasonably well the results presented here while the latter is

https://doi.org/10.1017/jfm.2013.545 Published online by Cambridge University Press

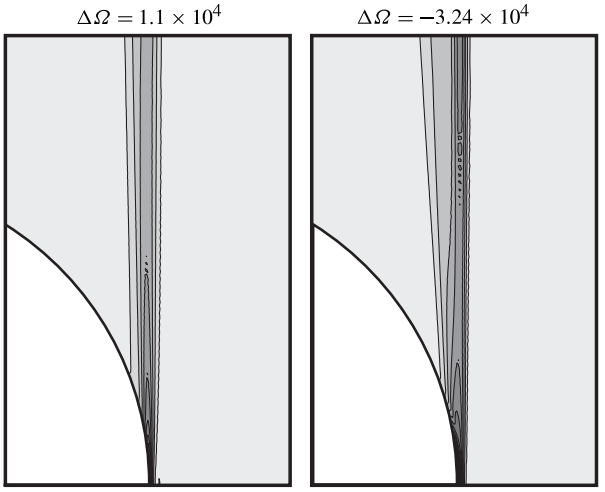


FIGURE 23. Contours of the azimuthally averaged non-axisymmetric kinetic energy for the super- and sub-rotation instabilities at $\Omega = 10^6$ illustrated in figure 22.

likely to be biased by the limited Ω values explored. Spherical Couette experiments by Schaeffer & Cardin (2005) in the regime $1.32 \times 10^4 \geqslant \Omega \leqslant 1.26 \times 10^5$ are consistent with the numerical results by Hollerbach (2003) and the simulations presented here.

In an asymptotic analysis Busse (1968) predicts the scaling $\Delta\Omega_c \sim \Omega^{1/4}$ for a free shear layer, ignoring the inner core and the outer boundary curvature. An asymptotic analysis by Schaeffer & Cardin (2005) for a split sphere geometry predicts $\Delta\Omega_c \sim \Omega^{1/2}$ and $m_c \sim \Omega^{0.25}$ when the outer boundary curvature is important. Their quasi-geostrophic numerical simulations confirm this scaling reasonably well. A split sphere is a full sphere where the shear is imposed by rotating the polar caps faster or slower than the remaining outer boundary.

Using numerical experiments, Hollerbach (2003) explores the reason for the differences between super- and sub-rotation instabilities in the spherical Couette system. He finds that the two instabilities become very similar in simulations without an inner core and follow the power law $\Delta\Omega_c \sim \Omega^{0.3}$. Hollerbach (2003) concludes that the abrupt height change due to the inner core influences the scaling and is responsible for the difference between super- and sub-rotation instabilities, at least for $\Omega < (1/3) \times 10^6$. Schaeffer & Cardin (2005) confirm this conjecture, using numerical but also experimental results. They compare their spherical shell experiments to experiments with a setup where the split sphere geometry is mimicked by two rotating discs located close to the outer boundary poles. Both experiments show clearly different results and only the spherical shell results are consistent with results presented here. The inner core influence thus explains why the full-sphere analysis by Busse (1968) or Schaeffer & Cardin (2005) fail to predict the onset in the spherical Couette system. Unfortunately, the experiments by Schaeffer & Cardin (2005) only reach $\Omega = 1.26 \times 10^5$ which is a factor 2.6 short of the value where the scaling should changed for sub-rotation cases.

3.4. *Inertial modes*

Inertial modes have previously been found in spherical Couette experiments (Kelley *et al.* 2007; Rieutord *et al.* 2012) and related numerical simulations (Matsui

https://doi.org/10.1017/jfm.2013.545 Published online by Cambridge University Press

et al. 2011; Rieutord *et al.* 2012). They are a solution of the inviscid linearized Navier–Stokes equation

$$\frac{\partial \boldsymbol{U}}{\partial t} = -\boldsymbol{\nabla} p - 2\Omega \hat{\boldsymbol{z}} \times \boldsymbol{U} \tag{3.11}$$

and are thus expected to be excited for large Ω (small Ekman number). In a full sphere, inertial modes can be formulated analytically and, following Kelley *et al.* (2007), the respective approach by Zhang *et al.* (2001) is adopted here. An inertial mode is characterized by its azimuthal wavenumber m and an additional wavenumber N that characterizes the complexity in z and s, the directions along and perpendicular to the rotation axis. For every m and N combination, there are $2N$ equatorially symmetric and $2N + 1$ equatorially antisymmetric modes with unique spatial patterns and unique frequencies σ. These modes are identified by an integer n according to the absolute frequency; $n = 1$ is the mode with the largest $|\sigma|$. The frequency is the result of a prograde or retrograde drift in azimuth and is defined as $\sigma = -m\omega_d/(2\Omega)$ in the inertial mode context where $\sigma = 1$ is the fastest possible mode. The slowest equatorially symmetric modes ($n = 2N$) are special. Their frequency is significantly lower than that of the other modes and they have a distinct quasi-geostrophic structure. These are the columnar Rossby modes which form a subset of general inertial modes in a sphere (Zhang *et al.* 2001).

Table 2 lists the drift for the instabilities discussed above and of inertial modes with similar geometry and/or matching σ. No inertial modes were found to resemble super-rotation instabilities for $\Omega < (1/3) \times 10^3$ and sub-rotation instabilities for $\Omega < (1/3) \times 10^4$ where viscosity effects and strong background flows faster than the outer boundary rotation are likely to lead to a system that is far from the inviscid linear Navier–Stokes equation. This is trivial for $\Omega = 0$ and still seems to hold for the sub-rotation helical instability found for $\Omega = 10^3$. One should keep in mind that the inner core, not present in the inertial mode solutions, may also contribute to modifying instabilities in the spherical Couette system.

Figure 24 illustrates the inertial modes that roughly match the instabilities found at $\Omega = 10^4$. A comparison with figure 19 reveals an overall similar structure but also demonstrates that the spherical Couette instabilities are modified by the background shear layer. For Rossby modes the inertial wavenumber N counts the column layers in the s-direction (Zhang *et al.* 2001). The rendering of these modes in figure 24 only highlights the inner, most energetic layer which seems to be promoted by the background zonal flows in the spherical Couette system. Other modifications concern the form of the columns and may also affect the drift, for example via advection (Schaeffer & Cardin 2005). The good frequency match between the geostrophic super-rotation instabilities and geostrophic inertial modes at $\Omega = 10^5$ and $\Omega = 10^6$ may thus only be a coincidence.

The selection of inertial modes in the tentative study presented here may indeed be somewhat arbitrary, in particular for the geostrophic sub-rotation instabilities. The full-sphere columnar Rossby modes always drift prograde while the sub-rotation spherical Couette instabilities always drift retrograde. Table 2 list inertial modes with frequencies close to $-\sigma_{SC}$, where σ_{SC} is the value in the spherical Couette solution. This choice is motivated by the fact that the geostrophic sub-rotation instabilities for $\Omega < (1/3) \times 10^6$ are mostly located inside the tangent cylinder. Since the height of the container decreases towards the rotation axis here, the β-effect is positive and leads to a retrograde rather than prograde drift. This argument does not hold for

https://doi.org/10.1017/jfm.2013.545 Published online by Cambridge University Press

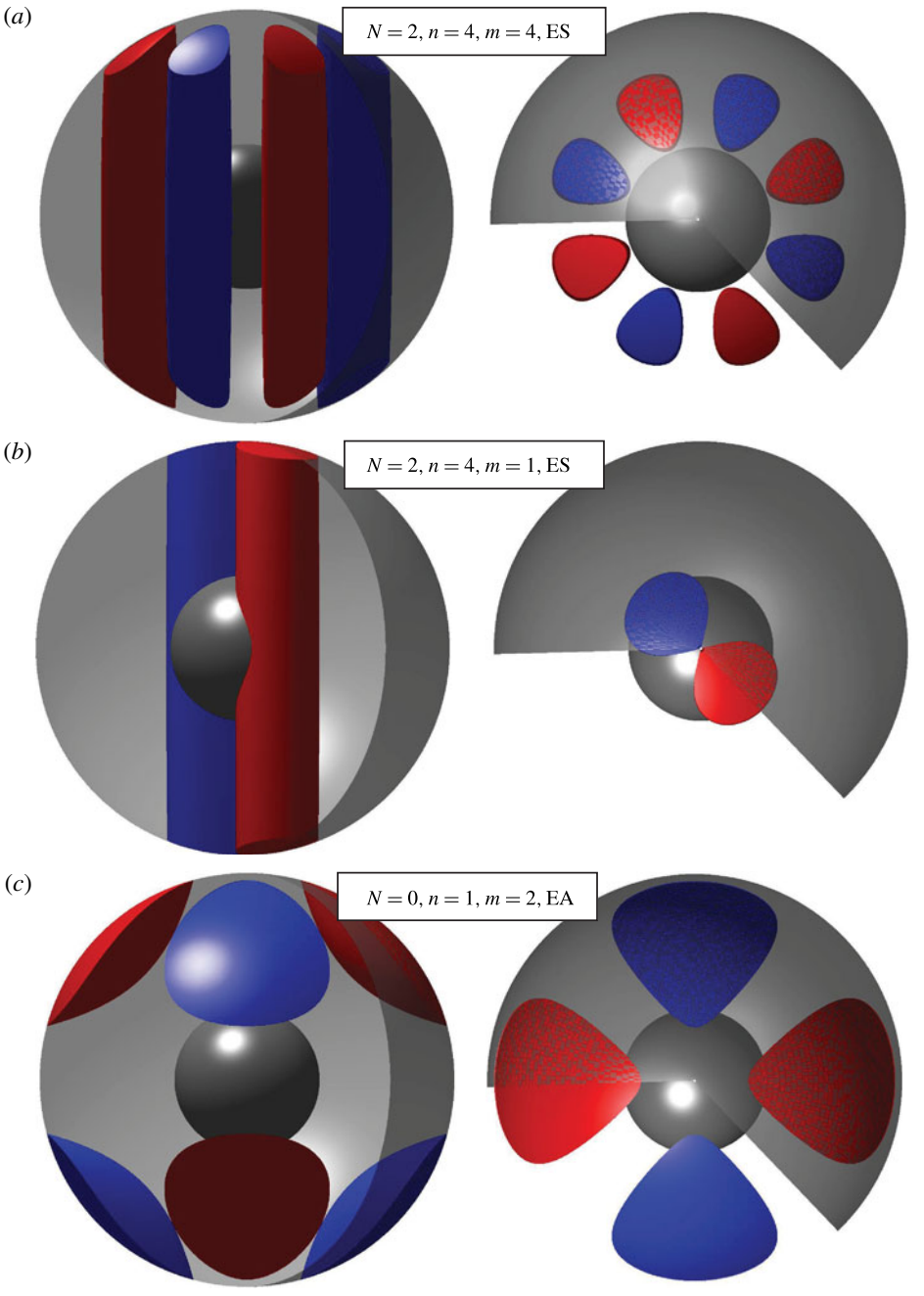


FIGURE 24. (Colour online) Inertial modes that roughly match the primary instabilities at $\Omega = 10^4$ illustrated in figure 19. Shown are isosurfaces of the flow component away from (red online) and towards (blue online) the rotation axis. Inertial modes are characterized by the wavenumbers N and m, by the additional ordering integer n and by their equatorial symmetry (ES = equatorially symmetric, EA = equatorially antisymmetric).

https://doi.org/10.1017/jfm.2013.545 Published online by Cambridge University Press

$\Omega \geqslant (1/3) \times 10^6$, however, where the sub-rotation instabilities set in just outside the tangent cylinder and nevertheless drift retrograde.

Schaeffer & Cardin (2005) suggest correcting the drift by the advection due to the background flow. This indeed leads to a prograde drift of sub-rotation instabilities at $\Omega < (1/3) \times 10^6$ but ignores the sign change in β and is also difficult to apply to super-rotation instabilities and sub-rotation instabilities at $\Omega < (1/3) \times 10^6$ that overlap with the complex Stewartson shear layer. Geostrophic Rossby modes are characterized by a nearly perfect balance between pressure gradient and Coriolis force and the consequence is their particularly slow drift (see (3.11)). The background flow may thus have a more pronounced influence than on faster inertial modes and could at least determine the drift direction, which would consistently explain the direction for all instabilities. Advection by the background flow may also, at least partly, explain the drift of the instabilities at smaller Ω values which are not inertial modes.

The case is more clear cut for the two equatorially antisymmetric fast inertial modes listed at the bottom of table 2. The dominant mode is illustrated in figure 24(*c*) which should be compared with figure 19(*d*) to reveal the similarity with the spherical Couette simulation. Both inertial modes have been found in the spherical Couette experiments (Kelley *et al.* 2007; Rieutord *et al.* 2012) and previous numerical simulations (Matsui *et al.* 2011; Rieutord *et al.* 2012). The full-sphere inertial mode with $(m = 2, N = 0, n = 1)$ has a frequency of $\sigma = 0.333$ while the dominant $m = 2$ contribution in the simulation has $\sigma_{SC} = 0.36$ at $\Omega = 10^4$ and $\Delta\Omega = -2 \times 10^4$. Rieutord *et al.* (2012) report a very similar frequency of $\sigma = 0.35$ for a spherical Couette experiment and inertial mode simulations in a spherical shell at $\Omega = 8.45 \times 10^6$ and $\Delta\Omega = -6.77 \times 10^6$. The secondary $m = 1$ mode has $\sigma_{SC} = 0.31$ while the matching full-sphere inertial mode $(m = 1, N = 1, n = 3)$ has $\sigma = 0.3060$. This is identical to the frequency reported by Rieutord *et al.* (2012) for $\Omega = 8.45 \times 10^6$ and $\Delta\Omega = -1.48 \times 10^7$. (Note that Kelley *et al.* 2007 and Rieutord *et al.* 2012 use the different notation introduced by Greenspan 1968 where $l = N + 3$ is the complexity parameter in the z- and s-directions.)

The frequencies of these modes are little affected by the presence of the inner core, probably because both are mainly localized closer to the outer boundary (Kelley *et al.* 2007). Rieutord *et al.* (2012) demonstrate that the frequency increases roughly linearly with $|\Delta\Omega|$ when increasing $|\Delta\Omega|$ beyond the critical value. A comparable dependence seems to hold for at least some of the instabilities reported here, as is demonstrated by the additional more supercritical values listed in table 2. It remains to be explored whether the increase is linear.

Refining the ideas of Kelley *et al.* (2007), Rieutord *et al.* (2012) suggest that a so-called critical layer may play an important role in the excitation of inertial modes in the spherical Couette system. This is cylindrical surface where the background flow angular velocity $\bar{\omega}$ matches the drift rate ω_d of the excited inertial mode within the Stewartson shear layer. For the fast Ω cases explored above $|\bar{\omega}|$ has a maximum of $0.5\,\Delta\Omega$ when $\Omega \leqslant 10^4$. The maximum increases to $\sim 0.6\,\Delta\Omega$ at $\Omega = (1/3) \times 10^7$. Rieutord *et al.* (2012) find that an inertial mode is excited when $\omega_d \leqslant 0.5\,\Delta\Omega$ or $\omega_d/\Delta\Omega \leqslant 0.5$ and report that this criterion allows the critical differential rotation $\Delta\Omega_c = 2\omega_d$ to be estimated for most of the fast inertial modes. The simulation presented here confirms this scenario for the $m = 2$ fast inertial mode. As reported by Rieutord *et al.* (2012), however, $\Delta\Omega_c$ is larger than $2\omega_d$ for the $m = 1$ mode. For most of the other instabilities discussed above, the ratio $\omega_d/\Delta\Omega$ remains clearly below 0.5, even very close to onset. The excitation via a critical layer remains an option but does not allow a simple prediction of the critical differential rotation rate for these modes.

https://doi.org/10.1017/jfm.2013.545 Published online by Cambridge University Press

The drift direction of geostrophic sub-rotation instabilities also poses a problem for the application of the critical layer theory.

4. Conclusion

The extensive study presented here provides an overview of the different instabilities in the wide-gap spherical Couette system for outer boundary rotation rates up to $\Omega = (1/3) \times 10^7$ (see figure 1). The results are consistent with the findings of previous numerical simulations and experiments that probed different sub-parts of the parameters space. Several new instabilities and the highly nonlinear behaviour are documented for the first time.

Viscous forces prevail for slow outer boundary rotation $\Omega \leqslant 1$. The first non-axisymmetric instabilities occur once the differential rotation (Reynolds number) reaches $\Delta\Omega_c \approx 1270$ with a respective r.m.s. flow Reynolds number of approximately 100. At this value the outer boundary rotation has lost its impact and the first non-axisymmetric mode is an instability of an equatorial jet, a thin nose of zonal flow attached to the inner sphere equator in combination with a concentrated radial outflow (Hollerbach 2003; Hollerbach *et al.* 2006; Guervilly & Cardin 2010). For intermediate Ω values and sub-rotation new double-roll and helical instabilities are found while super-rotation cases remain similar to those at slow Ω. For fast outer boundary rotation rates Coriolis effects enforce a quasi-two-dimensional fundamental flow with a complex Stewartson shear layer at the tangent cylinder (Stewartson 1966). This layer becomes unstable at Rossby numbers $Ro \leqslant 1$ where the outer boundary rotation remains important. For $\Omega \geqslant (1/3) \times 10^3$ and super-rotation or $\Omega \geqslant (1/3) \times 10^4$ and sub-rotation, the first non-axisymmetric instabilities are drifting geostrophic columns. They are similar to columnar Rossby modes, a type of particularly slow inertial mode that, for example, also characterize thermal convection in rotating spherical shells (Busse & Simitev 2004).

The geostrophic super-rotation instabilities have larger wavenumbers, tend to spread outside the tangent cylinder, and follow a clear power-law dependence on Ω. Sub-rotation instabilities, on the other hand, are characterized by small wavenumbers, remain confined to the region inside the tangent cylinder and show no simple dependence on Ω (Hollerbach 2003). This changes for very large rotation rates $\Omega \geqslant (1/3) \times 10^5$, however, where the sub-rotation seems to follow the same scaling as the super-rotation cases and both are of a very similar type. At least the azimuthal drift speed and the absolute critical differential rotation rates remain different, though. The higher absolute differential rotation required to drive the high-wavenumber sub-rotation instability seems to leave room for the low-wavenumber type to set in first when $\Omega < (1/3) \times 10^5$. A true understanding of the differences in super- and sub-rotation instabilities, however, is still missing. Numerical and laboratory experiments show that the presence of the inner core and the associated height change in the spherical shell container plays a role (Hollerbach 2003; Schaeffer & Cardin 2005).

As the absolute differential rotation is increased beyond $|\Delta\Omega_c|$ additional instabilities set in and lead to more complex spatial structures and first oscillatory, then chaotic time behaviour. In the large-Ω regime the scenario is complicated by a cascade to larger wavenumbers and intermittent oscillatory behaviour. Fast inertial modes, previously identified in spherical Couette experiments, appear for sub-rotation at $\Omega \geqslant 10^4$ around $Ro \approx 1$. For smaller Ω values these modes are damped by viscous effects. They are likely to be fed by the primary Stewartson layer instability, probably

https://doi.org/10.1017/jfm.2013.545 Published online by Cambridge University Press

via a critical layer (Rieutord *et al.* 2012). Why they only appear for sub-rotation and are always of the equatorially antisymmetric sub-type remains unclear. Since these inertial modes allow a direct comparison with experimental results a more detailed numerical study, preferential at larger Ω values, seems desirable.

Once $|\Delta\Omega|$ assumes values where $Ro \gg 1$ our simulations suggest that the Coriolis force generally loses its influence, even in the large-Ω regime. Equatorial-jet-type instabilities prevail and dominate Stewartson layer instabilities and inertial modes.

Appendix

Plugging the analytical solution for the axisymmetric toroidal flow equation (3.7) into (3.8) and using the ansatz

$$\Psi = g(r)\sin\theta\cos\theta \tag{A 1}$$

provides the fourth-order differential equation

$$\left(\frac{\partial^4}{\partial r^4} + \frac{4}{r}\frac{\partial^3}{\partial r^3} - \frac{12}{r^2}\frac{\partial^2}{\partial r^2} + \frac{24}{r^4}\right) g = 6\frac{(r_i/r)^3}{1-a^3}\left(\frac{(r_i/r)^3 - a^3}{1-a^3}\Delta\Omega^2 + \Omega\Delta\Omega\right). \tag{A 2}$$

This needs to be solved subject to the boundary conditions $\bar{\boldsymbol{U}}_P = 0$ at r_i and r_o which are fulfilled when

$$g = \frac{\partial}{\partial r}g = 0 \quad \text{at } r_i \text{ and } r_o. \tag{A 3}$$

Solution $g(r)$ can be written as the sum of the general homogeneous solution $h(r)$ and an inhomogeneous solution $k(r)$:

$$g(r) = h(r) + k(r). \tag{A 4}$$

The latter is relatively simple to determine:

$$k(r) = \frac{\Delta\Omega r_i^4}{4(1-a^3)^2}\left[\left(\Omega(1-a^3) - \Delta\Omega a^3\right)(r/r_i) - \Delta\Omega(r_i/r)^2\right]. \tag{A 5}$$

For the homogeneous solution we use the ansatz

$$h(r) = A(r/r_i)^2 + B(r/r_i)^4 + C(r/r_i)^{-1} + D(r/r_i)^{-3}. \tag{A 6}$$

The four boundary conditions (A 3) then serve to determine the four unknown coefficients:

$$\left.\begin{aligned} 2(1-a^3)A &= \;\; 7a^3(1-a^2)D - (4k_o - r_o k_o')a^2 + (4k_i - r_i k_i')a^3, \\ 5(1-a^2)B &= -2a^2(1-a^5)D - \;\; (k_o + r_o k_o')a^4 + \;\; (k_i + r_i k_i')a^2, \\ 5(1-a^3)C &= - \;\; 7(1-a^5)D + (4k_o - r_o k_o')a^2 - \;\; (4k_i - r_i k_i'), \end{aligned}\right\} \tag{A 7}$$

with $k_i = k(r_i)$, $k_o = k(r_o)$, $k_i' = \partial k(r_i)/\partial r$, and $k_o' = \partial k(r_o)/\partial r$. The remaining unknown coefficient D is given by

$$\begin{aligned} &\left(21(1-a^5)(1-a^2) - (4a^2(1-a^5) + 25(1-a^2))(1-a^3)\right) D \\ &\quad = 2\left((k_o + r_o k_o')a^4 - (k_i + r_i k_i')a^2\right)(1-a^3) \\ &\qquad + 3\left((4k_o - r_o k_o')a^2 - (4k_i - r_i k_i')\right)(1-a^2) + 5(2r_i - r_i k_i')(1-a^2)(1-a^3). \end{aligned} \tag{A 8}$$

https://doi.org/10.1017/jfm.2013.545 Published online by Cambridge University Press

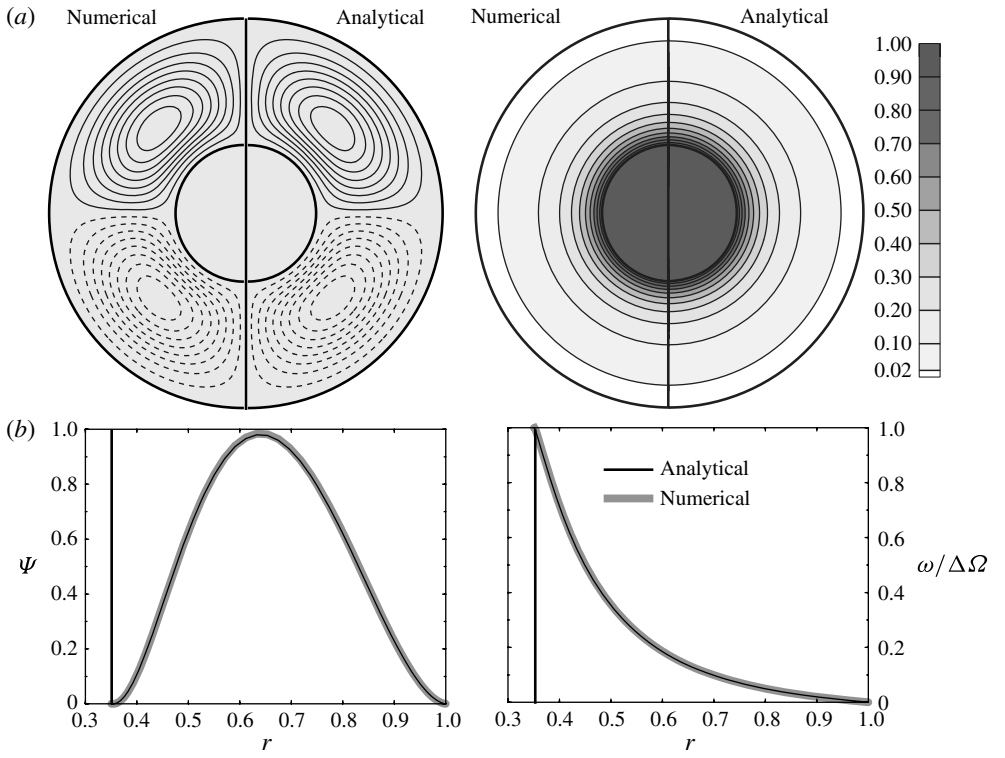


FIGURE 25. Comparison of the analytical and the numerical axisymmetric solutions at $\Omega = 10^{-4}$ and $\Delta\Omega = 10^{-6}$: (*a*) contour lines of Ψ, i.e. poloidal streamlines, on the left and the zonal angular velocity ω on the right; (*b*) profiles of Ψ and ω at a colatitude of $\sim 45°$.

Figure 25 shows a comparison of the analytical solution with the numerical one at $\Omega = 10^{-4}$ and $\Delta\Omega = 10^{-6}$ and demonstrates the perfect agreement.

REFERENCES

BRITO, D., ALBOUSSIÈRE, T., CARDIN, P., GAGNIÈRE, N., JAULT, D., LA RIZZA, P., MASSON, J.-P., NATAF, H.-C. & SCHMITT, D. 2011 Zonal shear and super-rotation in a magnetized spherical Couette-flow experiment. *Phys. Rev.* E **83** (6), 066310.

BUEHLER, K. 1990 Symmetries and asymmetric Taylor vortex flow in spherical gaps. *Acta Mechanica* **81**, 3–38.

BUSSE, F. H. 1968 Shear flow instabilities in rotating systems. *J. Fluid Mech.* **33**, 577–589.

BUSSE, F. H. & SIMITEV, R. 2004 Inertial convection in rotating fluid spheres. *J. Fluid Mech.* **498**, 23–30.

CAO, H., RUSSELL, C. T., WICHT, J., CHRISTENSEN, U. R. & DOUGHERTY, M. K. 2012 Saturn's high degree magnetic moments: evidence for a unique planetary dynamo. *Icarus* **221**, 388–394.

CHRISTENSEN, U. & WICHT, J. 2007 Numerical dynamo simulations. In *Core Dynamics* (ed. P. Olson), Treatise on Geophysics, vol. 8, pp. 245–282. Elsevier.

CHRISTENSEN, U. R., AUBERT, J., BUSSE, F. H., CARDIN, P., DORMY, E., GIBBONS, S., GLATZMAIER, G. A., HONKURA, Y., JONES, C. A., KONO, M., MATSUSHIMA, M., SAKURABA, A., TAKAHASHI, F., TILGNER, A., WICHT, J. & ZHANG, K. 2001 A numerical dynamo benchmark. *Phys. Earth Planet. Inter.* **128**, 25–34.

https://doi.org/10.1017/jfm.2013.545 Published online by Cambridge University Press

DORMY, E., CARDIN, P. & JAULT, D. 1998 MHD flow in a slightly differentially rotating spherical shell, with conducting inner core, in a dipolar magnetic field. *Earth Planet. Sci. Lett.* **158**, 15–24.

EGBERS, C. & RATH, H. J. 1995 The existence of Taylor vorticies and wide-gap instabilities in spherical Couette flow. *Acta Mechanica* **111**, 125–140.

FIGUEROA, A., SCHAEFFER, N., NATAF, H.-C. & SCHMITT, D. 2013 Modes and instabilities in magnetized spherical Couette flow. *J. Fluid Mech.* **716**, 445–469.

GLATZMAIER, G. A. 1984 Numerical simulation of stellar convective dynamos. 1. The model and methods. *J. Comput. Phys.* **55**, 461–484.

GREENSPAN, H. P. 1968 *The Theory of Rotating Fluids*. Breukelen Press.

GUERVILLY, C. & CARDIN, P. 2010 Numerical simulations of dynamos generated in spherical Couette flows. *Geophys. Astrophys. Fluid Dyn.* **104**, 221–248.

HOLLERBACH, R. 2003 Instabilities of the Stewartson layer. Part 1. The dependence on the sign of *Ro*. *J. Fluid Mech.* **492**, 289–302.

HOLLERBACH, R. 2009 Non-axisymmetric instabilities in magnetic spherical Couette flow. *Proc. R. Soc. Lond.* A **465**, 2003–2013.

HOLLERBACH, R., FUTTERER, B., MORE, T. & EGBERS, C. 2004 Instabilities of the Stewartson layer. Part 2. Supercritical mode transitions. *Theor. Comput. Fluid Dyn.* **18**, 197–204.

HOLLERBACH, R., JUNK, M. & EGBERS, C. 2006 Non-axisymmetric instabilities in basic state spherical Couette flow. *Fluid Dyn. Res.* **38**, 257–273.

KELLEY, D., TRIANA, S. A., ZIMMERMAN, D., TILGNER, A. & LATHROP, D. 2007 Inertial waves driven by differential rotation in a planetary geometry. *Geophys. Astrophys. Fluid Dyn.* **101**, 469–487.

MATSUI, H., ADAMS, M., KELLEY, D., TRIANA, S. A., ZIMMERMAN, D., BUFFETT, B. A. & LATHROP, D. P. 2011 Numerical and experimental investigation of shear-driven inertial oscillations in an Earth-like geometry. *Phys. Earth Planet. Inter.* **188**, 194–202.

PROUDMAN, I. 1956 The almost-rigid rotation of viscous fluid between concentric spheres. *J. Fluid Mech.* **1**, 505–516.

RIEUTORD, M., ANDRES TRIANA, S., ZIMMERMAN, D. S. & LATHROP, D. P. 2012 Excitation of inertial modes in an exerimental spherical Couette flow. *Phys. Rev.* E **86**, 026304.

RIEUTORD, M. & VALDETTARO, L. 1997 Inertial waves in a rotating spherical shell. *J. Fluid Mech.* **341**, 77–99.

SCHAEFFER, N. & CARDIN, P. 2005 Quasigeostrophic model of the instabilities of the Stewartson layer in flat and depth-varying containers. *Phys. Fluids* **17** (10), 104111.

SCHAEFFER, N. & CARDIN, P. 2006 Quasi-geostrophic kinematic dynamos at low magnetic Prandtl number. *Earth Planet. Sci. Lett.* **245**, 595–604.

STEWARTSON, K. 1966 On almost rigid rotations. Part 2. *J. Fluid Mech.* **26**, 131–144.

TAGG, R. 1994 The Couette–Taylor problem. *Nonlinear Sci. Today* **4** (3), 2–25.

WEI, X., JACKSON, A. & HOLLERBACH, R. 2012 Kinematic dynamo action in spherical Couette flow. *Geophys. Astrophys. Fluid Dyn.* **106**, 681–700.

WICHT, J. 2002 Inner-core conductivity in numerical dynamo simulations. *Phys. Earth Planet. Inter.* **132**, 281–302.

ZHANG, K., EARNSHAW, P., LIAO, X. & BUSSE, F. H. 2001 On inertial waves in a rotating fluid sphere. *J. Fluid Mech.* **437**, 103–119.

ZIMMERMAN, D. S., TRIANA, S. A. & LATHROP, D. P. 2011 Bi-stability in turbulent, rotating spherical Couette flow. *Phys. Fluids* **23** (6), 065104.

https://doi.org/10.1017/jfm.2013.545 Published online by Cambridge University Press